IN-PLANE CONDUCTIVE HEAT TRANSFER IN SOLID AND POROUS PLANAR STRUCTURES

BY
LASSE MIETTINEN

Academic Dissertation
for the Degree of
Doctor of Philosophy

To be presented, by permission of the
Faculty of Mathematics and Science
of the University of Jyväskylä,
for public examination in Auditorium FYS-1 of the
University of Jyväskylä on 17 December 2011
at 12 o'clock

Jyväskylä, Finland
December, 2011

Preface

The work reviewed in this Thesis was carried out during the years 2003-2011 in the Department of Physics at the University of Jyväskylä. There have been many setbacks along the way and few things have gone as planned, but I have learned a lot of physics and new skills during these years, also something about myself.

Jyväskylä, November 2011

Lasse Miettinen

ii

Abstract

Methods for determining the in-plane thermal diffusivity in a planar sample geometry were developed. These methods were tested and verified by measuring planar metal samples with known thermal properties. The techniques used were based on heating the sample at one edge and recording the evolution of the temperature field in the sample by a thermographic camera. The temperature fields at different times were processed and then fitted by a solution to a heat equation describing the experimental setup, thermal diffusivity as one of the fitting parameters.

In the first experimental setup the sample was placed in a weak constant flow of air, and the situation was improved in the second setup by placing the sample in a vacuum chamber, where convective heat transfer was totally removed. After verification measurements, the latter setup was applied to porous sintered bronze samples, and their effective thermal conductivities were determined. The sintered samples were also imaged by X-ray microtomography so as to obtain a 3D model for their structure. It was shown that the effective thermal conductivity of the samples could be predicted by an analytical expression which involved certain parameters determined from the 3D images.

Finally, as another application of the heat equation, propagation of temperature profiles in the form of slow-combustion fronts were studied in sheets of paper. The dynamical properties of these fronts belong to the KPZ universality class, for which theoretical results are available for the height-fluctuation distributions. Height fluctuations for such fronts were determined experimentally, and their distributions were found to be well fitted by corresponding theoretical distributions.

Keywords Thermal diffusivity, thermal conductivity, thermography, slow combustion, KPZ equation, height fluctuations

Author's address   Lasse Miettinen
Department of Physics
University of Jyväskylä
Finland

Supervisor   Professor Jussi Timonen
Department of Physics
University of Jyväskylä
Finland

Reviewers   Professor Pentti Saarenrinne
Energy and Process Engineering
Tampere University of Technology
Finland

Professor Timo Vesala
Department of Physics
University of Helsinki
Finland

Opponent   Professor Rinke J. Wijngaarden
Division of Physics and Astronomy
Vrije Universiteit
The Netherlands

List of Publications

Appendix I   MIETTINEN, L., MYLLYS, M., MERIKOSKI, J., AND TIMONEN, J., *Experimental determination of KPZ height-fluctuation distributions*, Eur. Phys. J. B **46** (2005) 55–60.

Appendix II   MIETTINEN, L., KEKÄLÄINEN, P., MERIKOSKI, J., MYLLYS, M., AND TIMONEN, J., *In-plane Thermal Diffusivity Measurement of Thin Samples Using a Transient Fin Model and Infrared Thermography*, Int. J. Thermophys. **29** (2008) 1422–1438.

Appendix III   MIETTINEN, L., KEKÄLÄINEN, P., MERIKOSKI, J., AND TIMONEN, J., *Measurement of the In-plane Thermal Diffusivity and Temperature-Dependent Convection Coefficient Using a Transient Fin Model and Infrared Thermography*, Int. J. Thermophys. **30** (2009) 1902–1917.

Appendix IV   MIETTINEN, L., KEKÄLÄINEN, P., TURPEINEN, T., HYVÄLUOMA, J., MERIKOSKI, J., AND TIMONEN, J., *Dependence of thermal conductivity on structural parameters in porous samples*. To be published.

The author of this Thesis has done the measurements, simulations, and data analysis of the article enclosed as Appendix I, and written the first draft of the article apart from its Introduction. The author has constructed and tested the experimental equipment, and acquired all the measurement data reported in articles II–IV. He has also performed the image analysis reported in article IV. The author of this thesis has also written the first versions of most parts of articles II–IV.

Contents

Chapter 1

Introduction

Porous materials form a large group of substances that are found both in nature and among man-made materials. Typical examples are wood, bone, many rocks, paper, concrete, filters, and insulators. All these have empty space, or pores, within them. The pores are usually filled with air or some other fluid, and the remainder is composed of the solid portion of the material.

Understanding heat transfer phenomena in such materials is important in many applications, but they are not however very well known. In this work we thus first concentrate on developing a measurement method for determining the in-plane thermal diffusivity of planar samples. This method is then applied to porous samples, and their effective thermal diffusivity (and conductivity) was determined. The three-dimensional structure of these samples was determined by X-ray tomography, which enabled their detailed characterization. By this way it is possible to analyze in a detailed manner the dependence of thermal conductivity on structural properties. Although numerical modeling of porous structures (especially packed beds of solid particles) has been developed [1–3], one has previously relied on experimental work when the effective thermal conductivity of porous materials has been needed [4–6].

The in-plane thermal conductivity of paper (or some other porous material) is an important parameter when analyzing the propagation of slow-combustion fronts in it. The properties of slow-combustion fronts can be shown to belong to the KPZ universality class [7,8].

As an application of heat conductivity in porous materials, we finally consider the height-fluctuation distributions of slow-combustion fronts in paper, and confirm that these distributions are those predicted for the KPZ universality class.

The three principal heat transfer mechanisms are conduction, convection and radiation. In addition to these three, transfer of latent heat may occur when first-order phase transition of a fluid medium is involved. An example of the latter mechanism is evaporation from a water pond. Some water molecules have enough energy to escape the liquid phase, whereby they remove thermal energy from the pond. Sit-

uations that include phase changes or mass transfer are not however considered in this work.

Heat transfer by conduction tends to equalize temperature gradients in the material via thermal motion of atoms. The governing equation of the conductive heat transfer is called Fourier's law. It states that the heat flux $\vec{q}$ is proportional to temperature gradient:

$$\vec{q}_{cond} = -k\vec{\nabla}T. \tag{1.1}$$

$T = T(x, y, z)$ is the temperature field and the proportionality constant k is the thermal conductivity characteristic of the material, where thermal conduction is taking place. Thermal conductivity is actually not strictly constant and depends usually on temperature.

Convective heat transfer relates to situations, where there is a fluid flow around an object, and their temperatures are different from each other. Newton's law of cooling gives the convective heat flux from a surface at temperature T_s surrounded by a fluid at temperature T_{env}:

$$q_{conv} = h(T_s - T_{env}). \tag{1.2}$$

Here constant h is the convection heat transfer coefficient, and the direction of the heat flux is normal to the surface. Equation (1.2) is exactly valid only locally. As the flow conditions vary at different parts of the surface, so will the convection heat transfer coefficient h and the heat flux q_{conv}.

Radiative heat transfer is different from the other two transfer mechanisms, because it does not require any medium. Heat is transferred by thermal radiation, usually at infrared (IR) wavelengths, from/to the surface of a body to/from the surroundings. All bodies at nonzero absolute temperature emit thermal radiation. The radiative heat flux emitted by a surface is determined by the equation

$$q_{rad} = \epsilon\sigma T_s^4, \tag{1.3}$$

where T_s is the surface temperature, σ the Stefan–Boltzmann constant ($5.67 \cdot 10^{-8}$ W$\cdot$m$^{-2}\cdot$K^{-4}), and $0 \leq \epsilon \leq 1$ the emissivity of the surface. For a perfect radiator, so called blackbody, $\epsilon = 1$. A surface not only emits radiation, it also absorbs radiation emitted by its surroundings or other heat sources. The absorption heat flux is given by the equation,

$$q_{abs} = \alpha\, q_{irr}, \tag{1.4}$$

where $0 \leq \alpha \leq 1$ is the absorptivity of the surface and q_{irr} is the thermal irradiation on the surface. When there are no extra heat sources present, the term q_{irr} is often approximated by blackbody radiation, $q_{irr} = \sigma T_{sur}^4$, at the temperature of the surroundings T_{sur}. The net radiative heat transfer rate from a surface is the difference of Eqs (1.3) and (1.4).

Heat transfer in a medium is described by the heat diffusion equation,

$$\rho c_p \frac{\partial T}{\partial t} = \frac{\partial}{\partial x}\left(k\frac{\partial T}{\partial x}\right) + \frac{\partial}{\partial y}\left(k\frac{\partial T}{\partial y}\right) + \frac{\partial}{\partial z}\left(k\frac{\partial T}{\partial z}\right) + \dot{q}$$
$$= \vec{\nabla}\cdot(k\vec{\nabla}T) + \dot{q}, \tag{1.5}$$

which is nothing more than a consequence of the conservation law of energy. Parameters ρ and c_p are the density and the specific heat at constant pressure of the material, respectively. The material parameters are often joined together as a single parameter $\alpha = k/\rho c_p$ called the thermal diffusivity. The energy generation rate per unit volume, $\dot{q}$, also includes possible heat losses from the system by convection, radiation, and (chemical) reactions. To solve the heat equation one needs to know an initial condition and two boundary conditions, in addition to the material parameters, because the partial differential equation is of first order in time and second order in space. Its solution is then a temperature field $T(x, y, z, t)$.

There are three common types of boundary conditions in heat transfer problems. The first type is the so called Dirichlet condition in which the temperature at the boundaries is known. A simple one-dimensional example is $T(L, t) = T_L$, where L is the location of the boundary in the x direction and T_L is the (possibly time-dependent) boundary temperature. The second type of boundary condition (also known as the von Neumann condition) states that the heat flux at a boundary is constant:

$$-k\left.\frac{\partial T}{\partial x}\right|_{x=L} = q_L. \tag{1.6}$$

Here the heat flux at the boundary q_L can also be zero for an insulated surface (adiabatic boundary). The third type of boundary condition is related to situations with convective heat transfer at a boundary surface:

$$-k\left.\frac{\partial T}{\partial x}\right|_{x=L} = h[T(L, t) - T_{env}]. \tag{1.7}$$

This equation states that heat is transferred from/to the surface by convection to/from the surrounding liquid or gas at temperature T_{env}, and an equal amount of heat has to be transferred by conduction in on solid side of the boundary.

All the heat-transfer and heat-loss mechanisms described above, as well as the boundary conditions, are involved in the thermal-conductivity measurements reported below.

The remainder of this Thesis is organized as follows. In Chapter 2 a new method for experimental determination of the in-plane thermal diffusivity of planar samples is described. Measurement results for copper and aluminum samples are presented as validation data. After a slight modification of the method, it was also shown to be applicable to a poorer thermal conductor, tantalum. In Chapter 3 the measurement

method is refined further in order to study samples that have a still lower thermal conductivity. A new measurement setup involving a vacuum chamber is presented together with the results of test measurements. After this, the measurement method is applied to porous sintered bronze plates in Chapter 4. The effective thermal conductivities determined for such samples are compared with theoretical expectations that involve certain structural parameters. These parameters are determined from three-dimensional tomographic reconstructions of the samples. In addition, the contact resistance between particles of which the samples are made can be included by performing lattice-Boltzmann simulations in the tomographic reconstructions of the samples. Chapter 5 expands the subject of heat transfer to height fluctuations in slow-combustion fronts in sheets of paper. Distributions of these fluctuations are compared with those predicted theoretically for the KPZ universality class. Finally, the work is summarized in Chapter 6.

Chapter 2

Thermal diffusivity measurements with convection present

In this section a method for determining the in-plane thermal diffusivity of planar samples is described. This method is based on measuring by using an infrared camera the transient temperature field of the sample heated at one edge. The temperature fields are spatially averaged over a narrow strip around the center line of the sample, and the temperature profiles for varying time are fitted by a solution to a corresponding one-dimensional heat equation. Two fitting parameters, the thermal diffusivity and the effective heat-loss term, are then obtained from time-dependent temperature data by optimization. With a known constant density and specific heat, the thermal conductivity of the sample can thus also be determined.

2.1   Background

There already exist many measurement methods for thermal diffusivity or thermal conductivity, see, e.g., [9]. The methods can be divided into steady-state and nonsteady-state methods according to time dependence of the measured temperature signal. The two categories can be further divided on the basis of, e.g., the geometry of the sample. Majority of the methods introduced in [9] concentrate on cylindrical sample geometries in either axial or radial heat flow. The quantities to be measured include temperature and in some cases also the heat flux, in addition to sample dimensions. If a comparative sample with known thermal conductivity is used, then the measurement of the heat flux can be avoided. The more recent methods take advantage of the development of thermography. With an infrared camera one can measure simultaneously both spatial distribution and time development of a two-dimensional temperature field. This is a big advantage over the use of individual temperature sensors.

The flash technique [10] is widely used (for a recent review, see [11]), and it is based on measuring temperature of the rear side of a planar sample with infrared

camera while the front side is heated with a flash lamp or a laser pulse. From the temperature evolution the thermal diffusivity in the thickness direction of the sample can be determined. The flash method has also been applied to determination of in-plane thermal diffusivity [12, 13]. However, in that case the signal-to-noise ratio has to be quite high (at least 10 [13]), which requires a sensitive infrared camera or a high heating temperature. The latter choice leads to complications with modeling the heat-loss effects.

We decided to design an experimental setup, where heating of the sample was realized by a simple heating element in contact with one end of the sample, while the temperature field was measured by an infrared camera. Instead of measuring the time evolution of temperature at two points like in Ref. [14], we used the whole temperature profile in a planar sample. To increase the accuracy of the method the convective and radiative heat transfer was modeled, and the linearized heat-loss coefficient was determined when determining the thermal diffusion coefficient. To this end, a weak flow of air was also induced around the sample to stabilize the convective heat transfer.

A motivation for using a simple heating element was that, by this method, a linear temperature front propagating in the sample can easily be produced. This measuring geometry allows one-dimensional modeling (provided that the sample can be regarded as isothermal in the thickness direction at all times), and different heat-loss mechanisms can more easily be included in the model.

2.2   Experimental setup

The experimental setup is shown schematically in Fig. 2.1. The sample that is being heated on one edge, is supported by pressing it between two heating elements. Under the sample there is a 100 mm diameter pipe and a fan, which are used to introduce a slow, laminar air flow over the plate in order to keep constant the convective heat transfer from the sample. A part of the pipe is filled with porous material to damp turbulence and to homogenize the air flow. The fan speed can be controlled. The velocity of the air flow at the exit of the pipe was measured with a hot wire anemometer, and it was found to be 0.1-0.2 m/s. This means that for a pipe 100 mm in diameter and air at 20°C the Reynolds number was about 1300 indicating laminar flow [15].

In the design of the experiment it was essential that the convective heat transfer could be kept as constant as possible. The whole experimental setup was therefore located in a room in which all disturbing air flows had been eliminated. But this alone was not sufficient and additional shielding around the measured sample had to be used. It turned out that shielding of the measuring chamber around the sample was necessary when good-quality temperature data were required. Without shielding, reflections of, e.g., hot equipment in the surroundings could be seen in

the temperature field of the sample, although it was painted black.
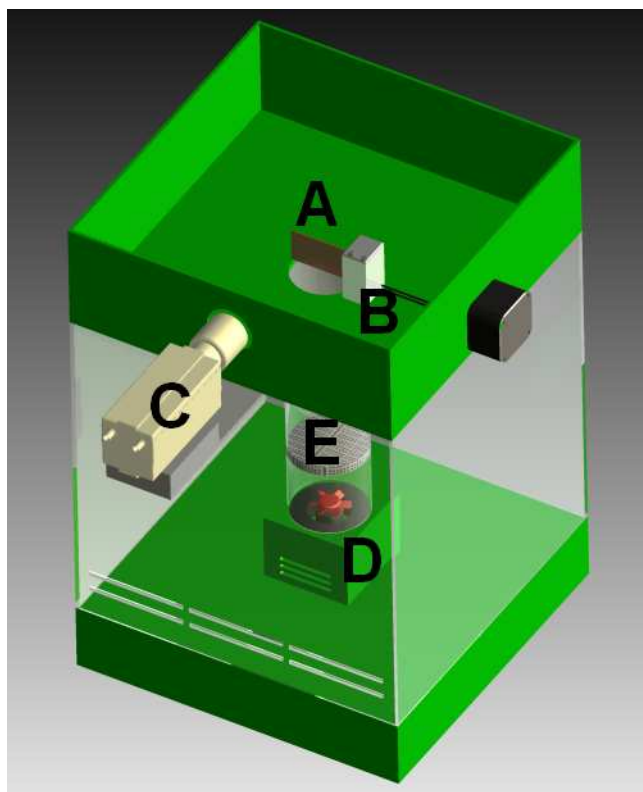
FIGURE 2.1 Schematic diagram of the experimental setup. The upper part of the measuring chamber is not shown. A is the sample, B is the heating unit, C is the IR camera, D is the fan, and E is the flow controller. Figure: Kimmo Ranttila.

A measurement was started by suddenly pressing the sample plate, initially at room temperature, between two copper plates heated by electric resistors. These resistors were covered by Teflon casings so as to minimize heat losses. The two heating resistors were connected in series, and the heating power could be adjusted. The time-dependent temperature field in the sample was recorded with an infrared camera, and a PC was connected to the camera for image grabbing and further data analysis. A total of 25 images per second were recorded in the measurements, and the pixel resolution of the measured temperature field was typically about 0.3 mm.

The emittance of the samples was improved by painting them thinly on both sides with black spray paint before measurements. The IR camera was then calibrated for each sample by attaching a thermocouple on the back surface of the sample, and measuring the temperature of that point on the front surface with the IR camera. The procedure was repeated for several different plate temperatures, and a calibration curve was eventually achieved. The emittance value was not determined because the calibration curve gives accurately the needed temperature data from the IR-camera images.

It was essential that the sample plate could be accurately cropped from the IR-

camera image. The temperature field was usually too blurred at the plate edges to distinguish the sample clearly from the background, especially at the cooler edge of the plate. Therefore, two electrically heated tungsten wires were attached vertically to a frame that was placed in front of the sample before beginning a measurement. The hot wires stood out from the background in the image, and with known distance between the wires, the position of the sample edges was determined accurately.

2.3 Mathematical model

Since a whole edge of the planar sample was heated and the boundary conditions were similar at the two adjacent plate edges, the system was symmetric in the transverse direction. Provided that sample thickness was much less than the ratio of the heat diffusion coefficient α to the effective heat-loss rate coefficient η (see below), i.e., that the relevant Biot number was much less than unity, we could also assume that the sample was isothermal in the thickness direction. Now we could have solved the remaining two-dimensional heat equation, but if we restricted our consideration to a narrow strip at the center line of the plate, we could use a one-dimensional heat equation to describe the system;

$$\rho c_p \frac{\partial T}{\partial t} = \frac{\partial}{\partial x}\left(k \frac{\partial T}{\partial x}\right) + \dot{q}. \tag{2.1}$$

Here $T = T(x, t)$ is the temperature of the plate with x the distance from the heated edge of the plate, c_p is the specific heat, ρ is the density, k is the thermal conductivity (more precisely the x component of the thermal-conductivity tensor) of the material of the plate, and $\dot{q}$ is the rate at which energy is generated (lost or gained) per unit volume of the medium. The energy generation term includes convective and radiative heat transfer;

$$\dot{q} \approx -\frac{2}{a}\left[h(T - T_\infty) + \epsilon\sigma(T^4 - T_{\text{sur}}^4)\right]. \tag{2.2}$$

Here a is the thickness of the plate, h is the convection heat transfer coefficient, ϵ is the emissivity, and σ is the Stefan–Boltzmann constant. T_∞ is the air temperature, and T_{sur} the temperature of the walls of the measuring chamber. In our case, $T_{\text{sur}} = T_\infty$. As temperature differences were quite small, we approximated the radiation term by a first-order term in $T - T_\infty$ such that

$$\frac{\partial \Theta}{\partial t} = \frac{\partial}{\partial x}\left(\alpha \frac{\partial \Theta}{\partial x}\right) - \frac{2}{a}\eta\Theta, \tag{2.3}$$

where $\Theta := T - T_\infty$, $\alpha = k/\rho c_p$ is the heat diffusion coefficient and $\eta := (h + 4\epsilon\sigma T_\infty^3)/\rho c_p$ is an effective heat-loss rate coefficient.

One edge of the plate was heated and the time-dependence of its temperature $\Theta(0, t)$ was measured. At the opposite edge we had convective and radiative heat transfer. So, in Eq. (2.3), we imposed the initial and boundary conditions

$$
\begin{cases}
\Theta(x, 0) = f(x), \\
\Theta(0, t) = \Theta_0(t), \\
\alpha \left. \dfrac{\partial \Theta}{\partial x} \right|_{x=L} + \eta\, \Theta(L, t) = 0,
\end{cases}
\tag{2.4}
$$

where L is the length of the plate. The initial temperature distribution $f(x)$ and the boundary temperature $\Theta_0(t)$ were obtained from measurements.

If α and η are constants, the boundary value problem can be solved analytically as described in Appendix A of the enclosed article II. The solution can be expressed in the form

$$
\begin{aligned}
\Theta(x, t) = \sum_{n=1}^{\infty} \frac{e^{-\alpha(\beta_n^2 + 2\eta/\alpha a)t}}{\gamma_n} & \left(\int_0^L f(y) \sin \beta_n y\, \mathrm{d}y \right. \\
& \left. + \alpha\, \beta_n \int_0^t e^{\alpha(\beta_n^2 + 2\eta/\alpha a)s}\, \Theta_0(s)\, \mathrm{d}s \right) \sin \beta_n x,
\end{aligned}
\tag{2.5}
$$

where

$$
\gamma_n = \frac{1}{2} \left(L + \frac{\eta/\alpha}{\beta_n^2 + (\eta/\alpha)^2} \right),
\tag{2.6}
$$

and $0 < \beta_1 < \beta_2 < \ldots$ are the solutions of the equation

$$
\frac{\eta}{\alpha}\, \tan \beta L = -\beta.
\tag{2.7}
$$

The unknown coefficients α and η can then be determined by minimizing the integral

$$
\int_{x_1}^{x_2} \left(\int_{t_1}^{t_2} \left(\Theta_{(\alpha,\, \eta)}(x, t) - \bar{\Theta}(x, t) \right)^2\, \mathrm{d}t \right) \mathrm{d}x
\tag{2.8}
$$

with respect to α and η. Here $\Theta_{(\alpha,\, \eta)}$ is the solution Eq. (2.5) and $\bar{\Theta}$ is the observed temperature. By this choice of the integral form we can take full advantage of the position and time information of the measured temperature data.

For a stationary temperature distribution, this two-dimensional optimization problem can be reduced into a one-dimensional problem in the following way. A stationary temperature distribution satisfies the differential equation

$$
\alpha \frac{\mathrm{d}^2 \Theta}{\mathrm{d}x^2} - \frac{2\,\eta}{a}\Theta = 0
\tag{2.9}
$$

with the boundary conditions

$$\begin{cases} \Theta(0) = \Theta_0 \\ \alpha \left.\dfrac{\mathrm{d}\Theta}{\mathrm{d}x}\right|_{x=L} + \eta\,\Theta(L) = 0. \end{cases} \tag{2.10}$$

Eq. (2.9) is a homogeneous second-order constant coefficient linear differential equation and it can be solved analytically. The solution that satisfies the boundary conditions (2.10) is

$$\Theta(x) = \Theta_0 \left(\frac{\cosh \beta(L-x) + (\eta/\alpha\beta)\sinh \beta(L-x)}{\cosh \beta L + (\eta/\alpha\beta)\sinh \beta L} \right), \tag{2.11}$$

where $\beta^2 = 2\eta/\alpha a$. From the data we get Θ_0 and the ratio η/α is determined by minimizing the integral

$$\int_{x_1}^{x_2} \left(\Theta_{\eta/\alpha}(x) - \bar{\Theta}(x) \right)^2 \mathrm{d}x, \tag{2.12}$$

where $\bar{\Theta}(x)$ is the measured stationary temperature profile. Because we now know the ratio of the two fitting parameters of the time-dependent case, Eq. (2.8), it is better to use η/α and α as the actual fitting parameters rather than η and α. The other reason for this choice is that the eigenvalues β_n in the solution of the time-dependent case (see Eq. (2.7)) are functions of η/α, and it is possible to save computation time by selecting this variable as a fitting parameter. The data were thus analyzed in the following way. Optimization with respect to the η/α parameter was done for the steady-state temperature profile (Eq. (2.12)). Thereafter a two-dimensional optimization of the time-dependent temperature profiles was performed (Eq. (2.8)) such that minimization was searched around the η/α value obtained for the steady-state profile.

2.4 Measurement results for good heat conductors

Homogeneous samples with known thermal-conductivity properties were used to validate the method. The sample plates were approximately 50 mm by 100 mm in size and 1.0 mm thick. There were two sample materials: high-purity copper and industrial aluminum (99.5 % pure). The known properties are shown for both materials in Table 2.1. In the mathematical model above, it was assumed that the thermal conductivity and the specific heat do not depend on temperature. These assumptions were well satisfied for the two materials because the temperature differences within the samples were relatively small.

A sample plate was initially at room temperature and was then suddenly

TABLE 2.1 Density, specific heat, thermal conductivity, and thermal diffusivity of the samples.

Sample	$\rho \ (\mathrm{kg \cdot m^{-3}})$	$c_p \ (\mathrm{J \cdot kg^{-1} \cdot K^{-1}})$	$k \ (\mathrm{W \cdot m^{-1} \cdot K^{-1}})$	$\alpha \ (10^{-3} \ \mathrm{m^2 \cdot s^{-1}})$
Cu	8940	385	399	0.1159
Al	2700	899	229	0.0943

pressed between two hot heating plates. Both the time-dependent and the subsequent steady-state temperature fields in the sample were recorded. Figure 2.2 shows a steady-state temperature field in a 1 mm thick copper plate. One-dimensional temperature profiles $T(x,t)$ (see Figs. 2.3 and 2.4) were obtained from the temperature fields by taking an average in the y direction over the central fifth of the sample. Noise in the resulting temperature profiles were reduced by taking a moving average over a 5-pixel (about 2 mm) wide window.
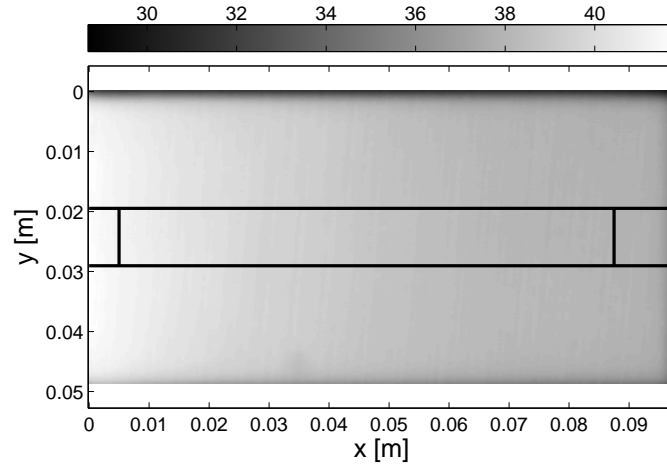

FIGURE 2.2 Steady-state temperature field (averaged over 30 s) of a copper plate recorded by an IR camera. The gray scale bar corresponds to temperature values in °C. The horizontal lines show the averaging window for which a one-dimensional temperature profile was calculated. The small vertical lines are the boundaries for fitting the temperature profile by theory.

A typical time evolution of the average temperature profile in a copper plate is shown in Fig. 2.4. The measured data were averaged over every five frames, i.e., over 0.2 s, to smooth the time evolution. The initial and boundary conditions, Eq. (2.4), for the solution of the heat equation, Eq. (2.3), were determined from the measured data. When fitting experimental data by Eq. (2.5), or by Eq. (2.11) in the steady state, about 10 mm stretches at the edges in the x direction were left out of the fit to eliminate edge effects.

After first finding the best fit $\Theta_{\eta/\alpha}(x)$ for the steady-state temperature profile (see Fig. 2.3), the minimum value of Eq. (2.8) for the time-dependent temperature
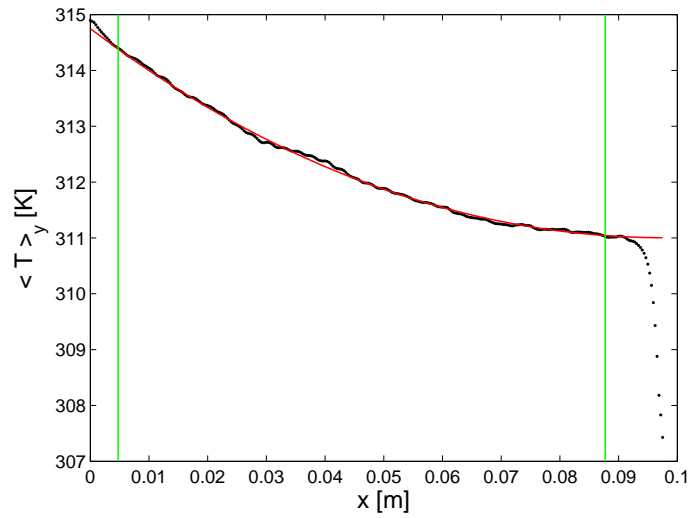
FIGURE 2.3 Steady-state temperature profile (dots) of a copper plate together with a theoretical fit by Eq. (2.11) (continuous line). The fitting window is between the two vertical lines. The best fit was found for the fitting-parameter value $\eta/\alpha = 0.0276\,\mathrm{m}^{-1}$. The air temperature was $T_\infty = 297.8\,\mathrm{K}$ in this measurement.
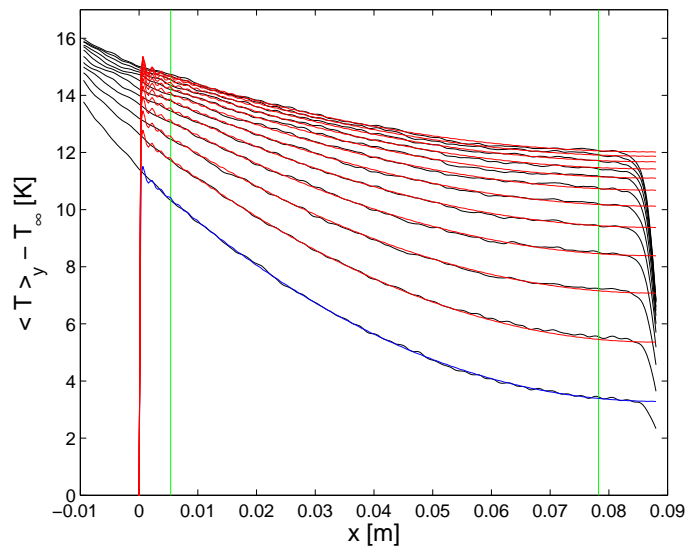
FIGURE 2.4 Transient average temperature profile of a copper plate at 10 s intervals. A fourth-order polynomial was fitted to the first (lowest) profile and was taken as the initial condition for the theoretical solution of the heat equation. The (time-dependent) boundary condition was taken at $x = 0$, and the two vertical lines show the integration region for optimization. The smooth lines for $x > 0$, $t > 0$ represent the theoretical solution, Eq. (2.5), with optimized values for η/α and α.

data was searched in the vicinity of the η/α value obtained for the steady-state profile. The contours of the cost function (2.8) for a copper sample, normalized by the integration area, are shown in Fig. 2.5. It turned out that, in this case, the minimum was found for $\eta/\alpha = 0.0274$ m^{-1} and $\alpha = 1.161 \times 10^{-4}$ m$^2 \cdot$s^{-1}. The η/α value obtained differed from the steady-state value of 0.0276 m^{-1} by 0.7 %. The bottom of the cost-function surface in the fitting parameter space was quite flat, as can be seen from the contours in Fig. 2.5, and finding the minimum accurately was sensitive to the η/α value.

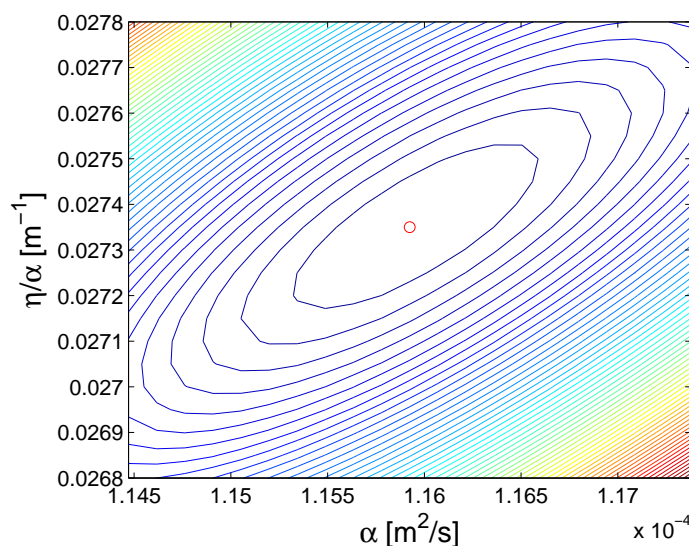**FIGURE 2.5** Normalized cost-function contours for a copper sample in the $(\alpha,\ \eta/\alpha)$ space. The small circle represents the location of the minimum. The values of the cost function on adjacent contour lines differ by 1 %.

Figure 2.6 shows the difference between the measured average temperature in a copper plate and the solution of the heat equation when using the best-fit parameter values $\eta/\alpha = 0.0274$ m^{-1} and $\alpha = 1.161 \times 10^{-4}$ m$^2 \cdot$s^{-1}. The square of this difference is actually integrated when determining the value of the cost function. The square root of the cost-function minimum gives a measure for the mean deviation between the theoretical solution and experimental data. In the case of Fig. 2.6, the minimum of the cost function normalized by the integration area was 0.00239 K^2, which means that the mean deviation of the solution from the measurement data was 0.05 K. This is actually less than the temperature resolution of the IR camera (0.1 K).

The procedure described above for determining the thermal diffusion coefficient of a sample was repeated for several independent copper measurements, and also for measurements on an aluminum plate. The results are shown in Table 2.2. The thermal-conductivity values were determined using the constant density and specific heat values of Table 2.1. The accuracy of the parameter η/α was 0.0001 m^{-1},
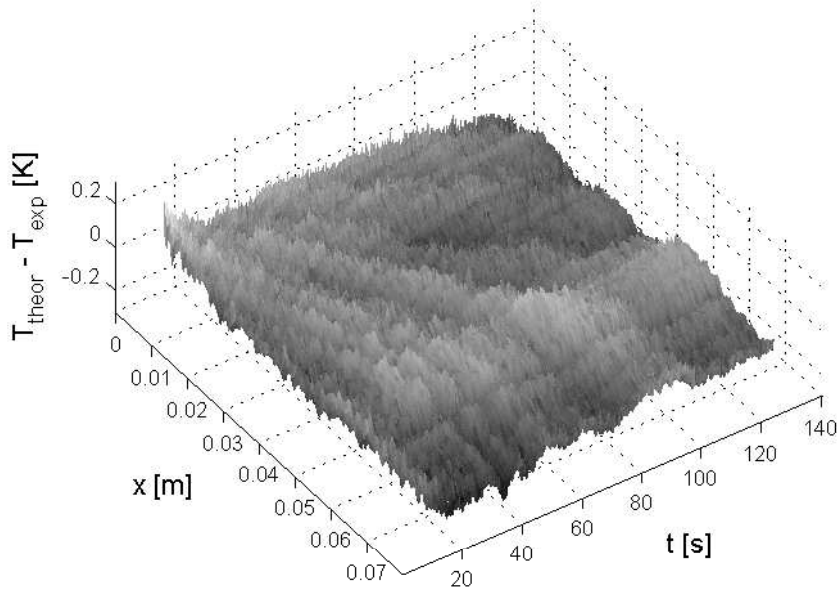
FIGURE 2.6 Difference between the measured temperature data for a copper sample and the theoretical solution of the heat equation calculated by using the best-fit values for the parameters η/α and α.

and it was $1.5 \times 10^{-7} \, \text{m}^2 \cdot \text{s}^{-1}$ for parameter α.

The error limits in the individual results of Table 2.2 are of the order of 0.5 %. This estimate was obtained by changing the integration limits and the moment when the initial temperature profile was taken from the measurement data. These changes moved the position of the cost-function minimum by about 0.5 % at the maximum. The mean values of the results shown in Table 2.2 are 401 and 220 $\text{W} \cdot \text{m}^{-1} \cdot \text{K}^{-1}$ for copper and aluminum, respectively. The corresponding values for the standard deviation of the mean are 3 and 1 $\text{W} \cdot \text{m}^{-1} \cdot \text{K}^{-1}$. Thus, the final results of our measurements are $401 \pm 3 \, \text{W} \cdot \text{m}^{-1} \cdot \text{K}^{-1}$ and $220 \pm 1 \, \text{W} \cdot \text{m}^{-1} \cdot \text{K}^{-1}$.

It was known from independent measurements that for the copper of which our sample was made, the thermal conductivity is $k = 399 \, \text{W} \cdot \text{m}^{-1} \cdot \text{K}^{-1}$ with unspecified error bars. This result is based on an electrical-conductivity measurement that is very accurate. Our result agrees well with this value. For the aluminum sample the measured thermal conductivity was only 4 % lower than the value shown in Table 2.1.

From Table 2.2 we can also calculate an average value for the parameter η, which consists of both convective and radiative parts as mentioned above. For the copper sample, $\eta \, \rho \, c_p = h + 4 \, \epsilon \, \sigma \, T_\infty^3 = 11.9 \pm 0.2 \, \text{W} \cdot \text{m}^{-2} \cdot \text{K}^{-1}$. The contribution of the radiation is about 50 %, and it cannot be ignored. Furthermore, we can now estimate how accurate the linearized temperature dependence of the radiation term is. For

TABLE 2.2 Results for individual measurements and averages for copper and aluminum. I_{norm} is the minimized value of the cost function (2.8) divided by the integration area.

Sample	η/α (m^{-1})	α (10^{-3} m$^2 \cdot$ s^{-1})	k (W$\cdot$m$^{-1}\cdot$K^{-1})	I_{norm} (K^2)
Cu	0.0284	0.1169	402.5	0.00304
	0.0306	0.1153	397	0.00415
	0.0294	0.1145	394	0.00314
	0.0274	0.1161	399.5	0.00239
	0.0293	0.1140	392.5	0.00305
	0.0295	0.1148	395	0.00317
	0.0304	0.1193	410.5	0.00311
	0.0311	0.1200	413	0.00288
	0.0308	0.1187	408.5	0.00338
	0.0296	0.1159	399	0.00361
average	0.0297	0.1165	401	0.00319
Al	0.0488	0.09002	218.5	0.00235
	0.0506	0.08919	216.5	0.00520
	0.0500	0.09084	220.5	0.00350
	0.0478	0.09084	220.5	0.00343
	0.0486	0.09125	221.5	0.00272
	0.0510	0.09187	223	0.00365
	0.0514	0.09105	221	0.00205
	0.0508	0.09084	220.5	0.00239
	0.0509	0.09105	221	0.00186
	0.0519	0.09187	223	0.00249
	0.0505	0.08981	218	0.00291
average	0.0502	0.09079	220	0.00296

the measurement shown in Figs. 2.3 and 2.4, the linearized form $4\,\epsilon\,\sigma\,T_\infty^3\,(T - T_\infty)$ gives an about 7 % lower heat flux (on the average) than the fourth-power term $\epsilon\,\sigma\,(T^4 - T_\infty^4)$ of the Stefan–Boltzmann law. This means a 0.5 % error in the flux per 1 K temperature difference between the plate and the surroundings. But for the fit parameter η, the error is only about 0.25 % $\cdot$ K^{-1}, and this effective temperature dependence is too low to detect when fitting the measurement data.

2.5 Towards poor heat conductors

The next step in the development of the measurement method was to extend it to moderate and poor heat conductors. For a relatively poorly conducting sample material, we chose tantalum as its thermal conductivity is constant over a wide temperature range around room temperature (see Table 2.3). We used two high-purity tantalum plates to study the thermal diffusivity and the temperature-dependent heat-loss coefficient. The thicknesses of the plates were 0.3 mm and 1.5 mm, and they were painted black on both sides.

TABLE 2.3 Density, specific heat, thermal conductivity, and thermal diffusivity of tantalum at some temperatures [9, p. 907]. The values at temperature 300 K were applied in this work.

T (K)	ρ (kg$\cdot$m^{-3})	c_p (J$\cdot$kg$^{-1}\cdot$K^{-1})	k (W$\cdot$m$^{-1}\cdot$K^{-1})	α (10^{-6} m$^2\cdot$s^{-1})
200	-	133	57.5	-
300	16600	140	57.5	24.7
400	-	144	57.8	-

It became evident that the two-dimensional temperature field in tantalum samples was not symmetric (see Fig. 2.7), as in copper and aluminum samples. The reason for this asymmetry was traced to the alignment of the sample perpendicular to the weak flow of air used. The velocity boundary layer that forms on the plate surface grows along the flow direction. The flow velocity is the largest at the lower edge of the plate, and there the convective heat transfer is stronger than at the upper (trailing) edge. For poor heat conductors this obviously leads to an asymmetric temperature field. A simple remedy to this problem was to place the sample parallel to the upward-going air flow with the heated edge up. The heater was placed up because of practical reasons and because then the additional natural convection caused by heating does not interfere too much with the measurement. This setup indeed resulted in a symmetric temperature field, and a one-dimensional temperature profile could again be determined by averaging over a narrow strip around the center line of the sample (see Fig. 2.8 on page 21). Other than the sample alignment, the measurement procedures remained as described in sections 2.2 and 2.4.
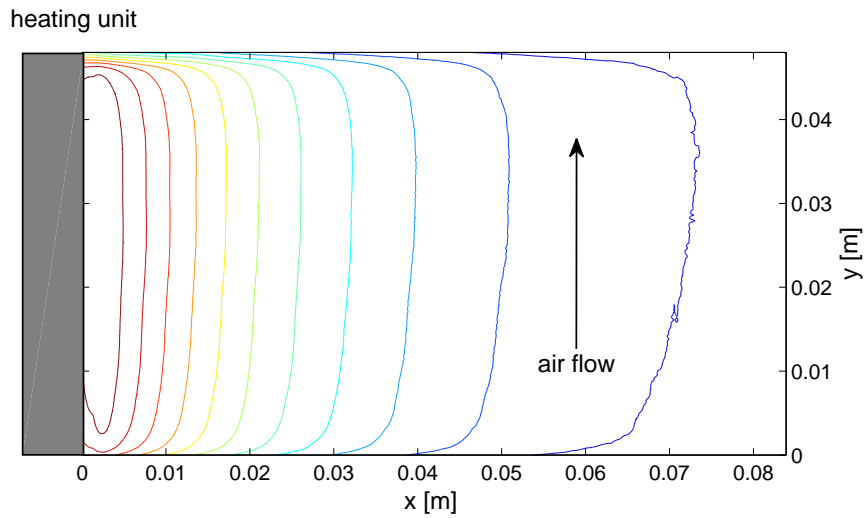
FIGURE 2.7 Isotherms of a stationary temperature field measured on the 0.3 mm thick tantalum sample. The direction of the air flow is indicated. The temperature field does not remain symmetric with respect to the center line in the x direction of the sample.

The change in the sample alignment led, however, to a problem with the model introduced in section 2.3 where it was assumed that the heat transfer by convection would be constant in the direction in which the temperature profile was averaged. Now that air was flowing parallel to the gradient of the temperature profile, this assumption was no longer valid: the velocity and thermal boundary layers were increased towards the hot end of the sample, and, consequently, the convective heat transfer coefficient was also changing. The position dependence of this coefficient had thus to be taken into account, and we modeled the effect by introducing a temperature-dependent coefficient. This meant that the transient fin model became nonlinear, and a new solution to it had to be found.

2.6   Mathematical model of the improved experimental setup

The starting point is the same as before: we restrict our consideration to a narrow strip around the center line of the sample plate, and use a one-dimensional transient fin model to describe the system. So, Eqs (2.1) and (2.2) with $T_{\text{sur}} = T_\infty$ and constant values of the material parameters ρ, c_p, and k lead to the equation

$$\rho c_p \frac{\partial T}{\partial t} = k \frac{\partial^2 T}{\partial x^2} - \frac{2}{a} \left[h \cdot (T - T_\infty) + \epsilon\sigma \cdot (T^4 - T_\infty^4) \right].$$ (2.13)

The only difference to the earlier is that the convective heat-transfer coefficient h is now position dependent, $h = h(x)$, because of the boundary-layer effects on the

air flow across the plate. The temperature of the plate in a stationary situation is described by the equation

$$k \frac{\mathrm{d}^2 T}{\mathrm{d}x^2} - \frac{2}{a} \left[h(x)(T - T_\infty) + \epsilon\sigma(T^4 - T_\infty^4) \right] = 0 \tag{2.14}$$

with the boundary conditions

$$\begin{cases} T(0) = T_0 \\ k \left.\frac{\mathrm{d}T}{\mathrm{d}x}\right|_{x=L} + h(L)\left(T(L) - T_\infty\right) + \epsilon\sigma\left(T(L)^4 - T_\infty^4\right) = 0, \end{cases} \tag{2.15}$$

where L is the length of the plate and T_0 is a measured boundary temperature. The functional dependence $h = h(x)$ is a priori unknown, and cannot be solved by standard methods applied [16] in the case of a homogeneous temperature in the sample plate (in which case one finds $h(x) \propto x^{-1/2}$; we also checked that experimental data were not consistent with this kind of position dependence in $h(x)$). We can, however, circumvent this problem as the temperature profile $T = T(x)$ is a monotonic function, and we thus have a one-to-one correspondence between x and T, or rather x and $\Theta = T - T_\infty$. This means that we can also consider x as a function of Θ, $x = x(\Theta)$. We can thus express Eq. (2.14) in the form

$$k \frac{\mathrm{d}^2 T}{\mathrm{d}x^2} - \frac{2}{a} \left[h(\Theta)(T - T_\infty) + \epsilon\sigma(T^4 - T_\infty^4) \right] = 0 \tag{2.16}$$

with an unknown function $h = h(\Theta)$. Since the temperature range in the plate is quite narrow, we can also replace $h(\Theta)$ by its first-order approximation,

$$h(\Theta) = h_0 + h_1\Theta, \tag{2.17}$$

where h_0 and h_1 are, in principle, functions of T_∞. Variation of T_∞ is, however, so small in the experiments that they can be considered here as constants. This kind of approach has also been used before [17].

Substituting the expression Eq. (2.17) into Eq. (2.16), expanding the term $T^4 - T_\infty^4$ as a Taylor series with respect to $\Theta = T - T_\infty$ and retaining only its first two terms, Eq. (2.16) becomes

$$\alpha \frac{\mathrm{d}^2\Theta}{\mathrm{d}x^2} - \frac{2}{a} \frac{h_0 + 4\epsilon\sigma T_\infty^3 + (h_1 + 6\epsilon\sigma T_\infty^2)\Theta}{\rho c_p}\Theta = 0. \tag{2.18}$$

We can define

$$\eta := \eta(\Theta) = \eta_0 + \eta_1\Theta = \frac{h_0 + 4\epsilon\sigma T_\infty^3}{\rho c_p} + \frac{h_1 + 6\epsilon\sigma T_\infty^2}{\rho c_p}\Theta \tag{2.19}$$

as an effective temperature-dependent heat-loss coefficient that includes both convective and radiative heat transfer. With this notation, the stationary temperature profile of the plate is determined by

$$\alpha \frac{\mathrm{d}^2\Theta}{\mathrm{d}x^2} - \frac{2}{a}(\eta_0 + \eta_1\Theta)\Theta = 0. \tag{2.20}$$

The boundary conditions are now

$$\begin{cases} \Theta(0) = \Theta_0 \\ \alpha \left.\frac{\mathrm{d}\Theta}{\mathrm{d}x}\right|_{x=L} + (\eta_0 + \eta_1\Theta(L))\,\Theta(L) = 0. \end{cases} \tag{2.21}$$

This boundary-value problem can most easily be solved numerically. The two unknown coefficients, η_0/α and η_1/α, can be determined by minimizing the integral

$$\int_{x_1}^{x_2} \left(\Theta_{(\eta_0/\alpha,\,\eta_1/\alpha)}(x) - \bar{\Theta}(x)\right)^2 \mathrm{d}x \tag{2.22}$$

with rescpect to η_0/α and η_1/α. Here $\Theta_{(\eta_0/\alpha,\,\eta_1/\alpha)}$ is a solution to the boundary-value problem, Eq.(2.20) with Eq. (2.21), and Θ is the measured stationary temperature profile.

The time-dependent case, Eq. (2.13), can also be written in a similar form,

$$\frac{\partial\Theta}{\partial t} = \alpha \frac{\partial^2\Theta}{\partial x^2} - \frac{2}{a}\left(\eta_0 + \eta_1\Theta\right)\Theta. \tag{2.23}$$

Notice that Eq. (2.23) is a nonlinear partial-differential equation. In the experiments one edge of the plate was heated and the time dependence of the edge temperature, $\Theta(0,t)$, was measured. At the opposite edge we had convective and radiative heat transfer. So, in Eq. (2.23), we imposed the initial and boundary conditions

$$\begin{cases} \Theta(x,0) = f(x), \\ \Theta(0,t) = \Theta_0(t), \\ \alpha \left.\frac{\partial\Theta}{\partial x}\right|_{x=L} + (\eta_0 + \eta_1\Theta(L,t))\,\Theta(L,t) = 0. \end{cases} \tag{2.24}$$

The initial temperature profile $f(x)$ and the time-dependent edge temperature $\Theta_0(t)$ are known (measured) functions.

Once the parameters η_0/α and η_1/α were extracted from the stationary temperature profile, the transient case, Eq. (2.23) with Eq. (2.24), could be solved numerically. Now there was, in principle, only one independent unknown parameter left, the thermal diffusivity, α. But, as in the earlier case with constant convective heat-transfer coefficient, we searched for an optimal solution to the transient problem by letting the η_0/α value obtained from the stationary data vary around the stationary

value, and had thereby two fitting parameters also in the transient case, α and η_0/α. Only the parameter η_1/α was taken as such from the stationary case. Variation of η_1/α would have been a higher-order effect.

Experimental data were thus analyzed in the following way. Two-dimensional optimization with respect to parameters, η_0/α and η_1/α, was performed for the steady-state temperature profile, Eq. (2.22), as described above. Thereafter, a two-dimensional optimization by minimizing

$$\int_{x_1}^{x_2} \left(\int_{t_1}^{t_2} \left(\Theta_{(\alpha,\,\eta_0/\alpha)}(x,t) - \bar{\Theta}(x,t) \right)^2 \, \mathrm{d}t \right) \, \mathrm{d}x \tag{2.25}$$

for the time-dependent temperature profiles $\Theta(x,t)$ was performed with respect to α and η_0/α. The minimum value of Eq. (2.25) was searched in the vicinity of the η_0/α value obtained for the steady-state profile.

2.7   Results of the tantalum measurements

It turned out that in transient measurements the temperature rise in the 0.3 mm thick tantalum plate was too small to reliably determine the location of the minimum of the cost function of Eq. (2.25) in the two-dimensional parameter space. It also became clear that changes in the temperature profile of the 1.5 mm thick sample were too small in the stationary state for optimization by Eq. (2.22). For these reasons we measured and analyzed only the stationary temperature profile in the 0.3 mm thick sample and the transient temperature profile in the 1.5 mm thick sample. The same conclusion can also be made based on a sensitivity analysis (see, e.g., [17]) of the heat equation with respect to the fitting parameters. The analysis is conducted in section 4 (Sensitivity Analysis) of the enclosed article III.

An example of a stationary temperature field in the 0.3 mm thick tantalum plate is shown in Fig. 2.8. Isothermal contours show clearly the symmetry of the field, and the window in the vertical direction (x axis), in which the temperature is averaged over the y direction, is marked by straight lines. The resulting mean temperature profile in the x direction is shown in Fig. 2.9 together with the best theoretical fit based on Eqs (2.20)–(2.22). The fitted interval in the x direction is indicated by short horizontal lines in Fig. 2.8, i.e., 10-mm-long intervals at both edges were left out of the fit. The inset in Fig. 2.9 shows the difference between the data and the fit in more detail. For comparison the corresponding difference is also shown for a linear fin model (see section 2.3) where the convective heat-transfer coefficient does not depend on temperature. It is evident that the model with the temperature-dependent coefficient provides a better fit. For various stationary measurements with tantalum the minimum value of the cost function was reduced by 64 % to 88 % compared to that of the linear fin model. For the measurement of Fig. 2.9, the parameters that
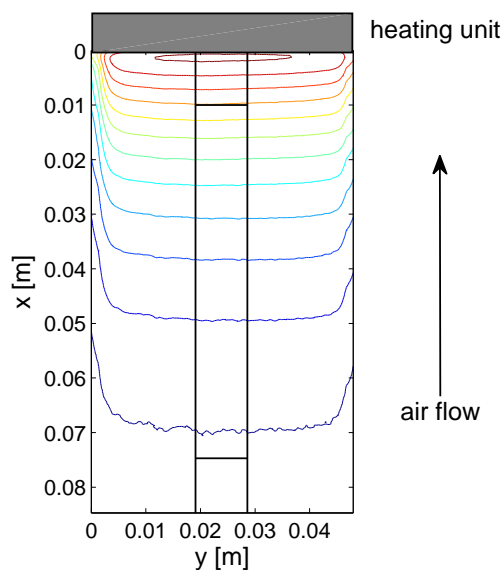
FIGURE 2.8 Isotherms of a stationary temperature field measured on the 0.3 mm thick tantalum sample. The direction of the air flow is indicated. The field was obtained by time averaging over all saved infrared camera frames in the stationary regime. The vertical lines border the window in which the mean temperature profile in the x direction was determined. The short horizontal lines indicate the interval in the x direction in which the temperature profile of Fig. 2.9 was fitted by the stationary fin model.

gave the best fit were $\eta_0/\alpha = 0.10693$ m^{-1} and $\eta_1/\alpha = 0.00503$ m$^{-1} \cdot$ K^{-1}, as indicated by the contour lines of the cost function, Eq. (2.22), shown in Fig. 2.10.

The fitted results for all the stationary temperature data measured are listed in Table 2.4. The same results are shown graphically in Fig. 2.11, where the ratio of the effective heat-loss coefficient (see Eq. (2.19)) to thermal diffusivity is plotted as a function of temperature. Each line corresponds to a result measured in the temperature range given by the end points of the line. The lengths and positions of the lines are thus variable. From Table 2.4 the averaged final results for the two fitting parameters are $\eta_0/\alpha = (0.121 \pm 0.003)$ m^{-1} and $\eta_1/\alpha = (0.0044 \pm 0.0002)$ m$^{-1} \cdot$ K^{-1}. The error estimates are based on the standard deviation of the mean. The value for the temperature-dependent part of the effective heat-loss coefficient, η_1/α, was used later in the numerical solution of the transient fin model.

Time-dependent temperature profiles from a single measurement in the 1.5 mm thick tantalum plate are shown in Fig. 2.12 with 12 s intervals. Also plotted in this figure is the best fit by a numerical solution of the transient fin model, Eq. (2.23), with Eq. (2.24). As in the stationary case, the last 10 mm of the experimental temperature profile data were left out when optimizing the cost function, Eq. (2.25). Since the differences between the experimental and numerical data were so small, they are shown separately in Fig. 2.13. They are of the order of 0.1 K at maximum, which is also the accuracy of the IR camera.
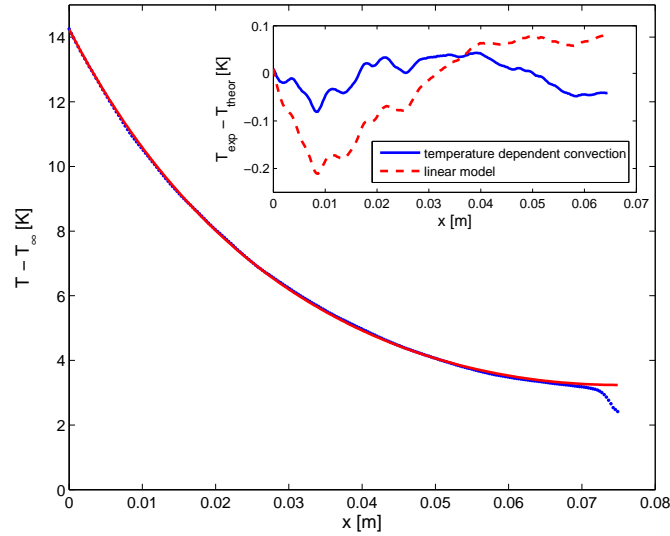
FIGURE 2.9 The stationary temperature profile from the data of Fig. 2.8 (dots) smoothed by a nine-point moving average. The ambient temperature $T_\infty = 297.8$ K has been subtracted. Note that the first 10 mm interval in the x direction of Fig. 2.8 is omitted, and the origin has been shifted accordingly. The solid line represents the best fit by numerically solving the stationary fin model, Eqs (2.20)–(2.22). The last 10 mm interval of the measured profile was not used in the optimization. The differences between the data and the fit are shown in the inset for two different fin models. The dashed line is the result for the linear model of section 2.3 while the solid line is the result for the improved fin model with a temperature-dependent convection coefficient.

TABLE 2.4 Fitted parameter values for the stationary temperature measurements on the 0.3 mm thick tantalum sample, and measured temperature of air flow.

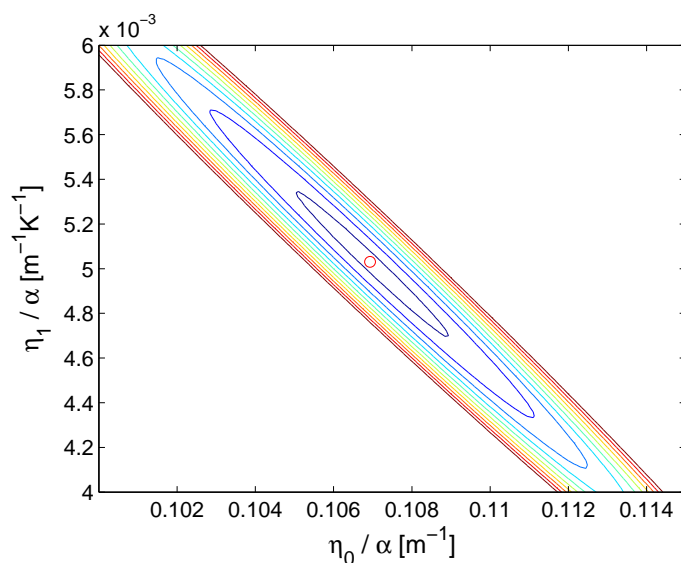| Measurement	η_0/α (m^{-1})	η_1/α (m$^{-1} \cdot$K^{-1})	T_∞ (K)
1	0.11869	0.00501	298.7
2	0.12033	0.00398	298.5
3	0.12262	0.00402	298.4
4	0.11360	0.00462	298.6
5	0.11708	0.00442	298.7
6	0.12083	0.00422	298.6
7	0.13123	0.00417	297.9
8	0.13829	0.00357	298.1
9	0.12366	0.00505	298.2
10	0.10693	0.00503	297.8
average	0.12133	0.004409	298.35

FIGURE 2.10 Contour lines of the cost function, Eq. (2.22), for the stationary temperature profile of Fig. 2.9. The best fit is provided by the parameter values, $\eta_0/\alpha = 0.10693\,\mathrm{m}^{-1}$ and $\eta_1/\alpha = 0.00503\,\mathrm{m}^{-1}\cdot\mathrm{K}^{-1}$. The location of the minimum is marked by a small circle. The value of the cost function on the innermost contour line is 3 % larger than the minimum value; on the second contour line, it is 13 % larger; and thereafter, lines indicate an additional 10 % unit increase in the value.
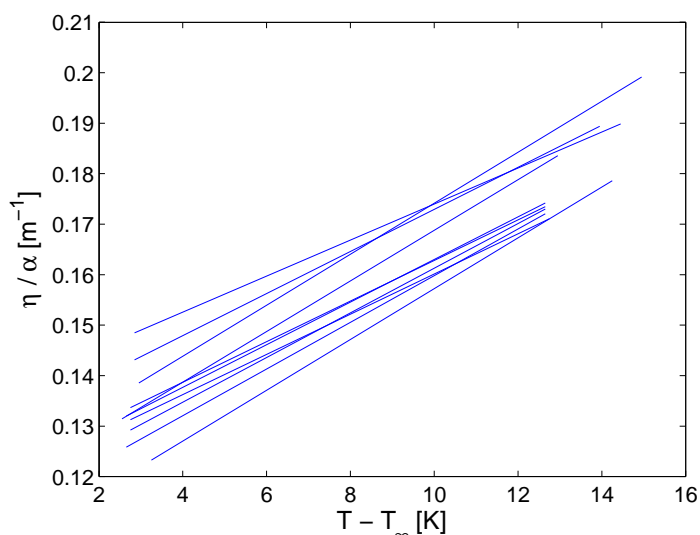

FIGURE 2.11 Results of Table 2.4 in a graphical form, i.e., $\frac{\eta}{\alpha} = \frac{\eta_0}{\alpha} + \frac{\eta_1}{\alpha}(T - T_\infty)$ as a function of temperature for each individual measurement.

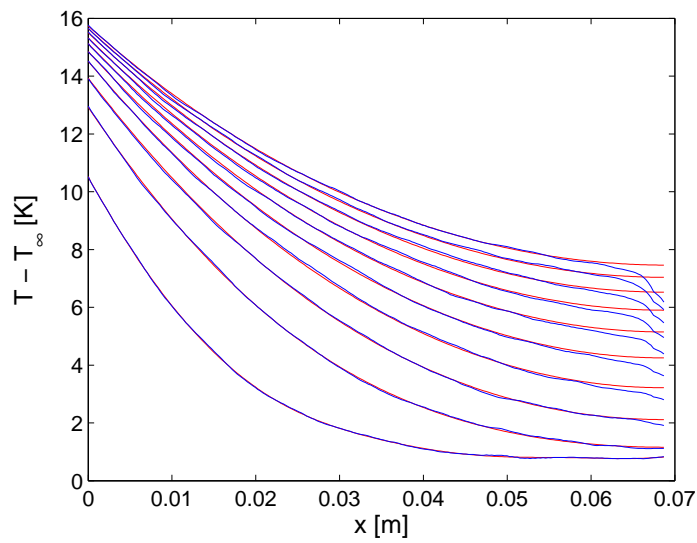**FIGURE 2.12** Transient temperature profiles in the 1.5 mm thick tantalum plate at 12 s intervals together with the best fit by a numerical solution of the transient fin model, Eq. (2.23) with Eq. (2.24). The last 10 mm interval of the measured profile was not used in the optimization.
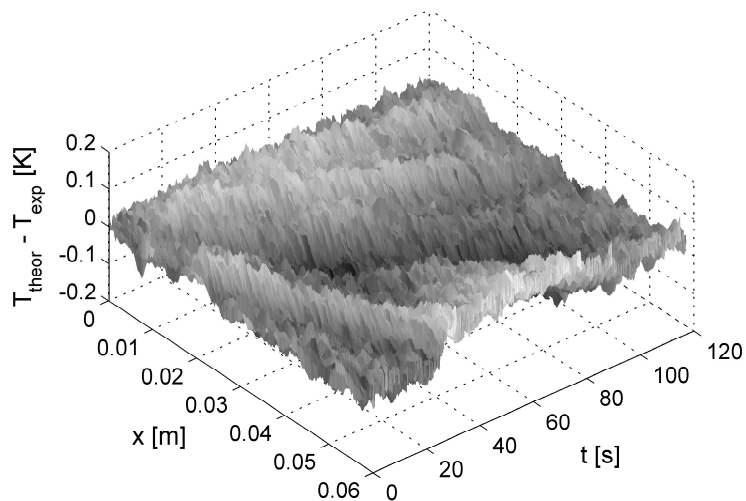

FIGURE 2.13 Difference between the best fit and the measured data of Fig. 2.12 within the optimization region.

The contour lines of the cost function, Eq. (2.25), are shown in Fig. 2.14 for the transient temperature data of Fig. 2.12. In the cost function the parameters were α and η_0/α, but we actually used the thermal conductivity k as a fitting parameter instead of the thermal-diffusion coefficient α, using the known values for the density and specific heat of the tantalum shown also in Table 2.3. A comparison to the result of the linear transient fin model was also made for this measurement. The minimum of the cost function was 30 % higher when the linear model was used. This is another indication that the temperature-dependent convection coefficient must be used when fitting the data, although the difference between the models is lower than in the case of the stationary data above.
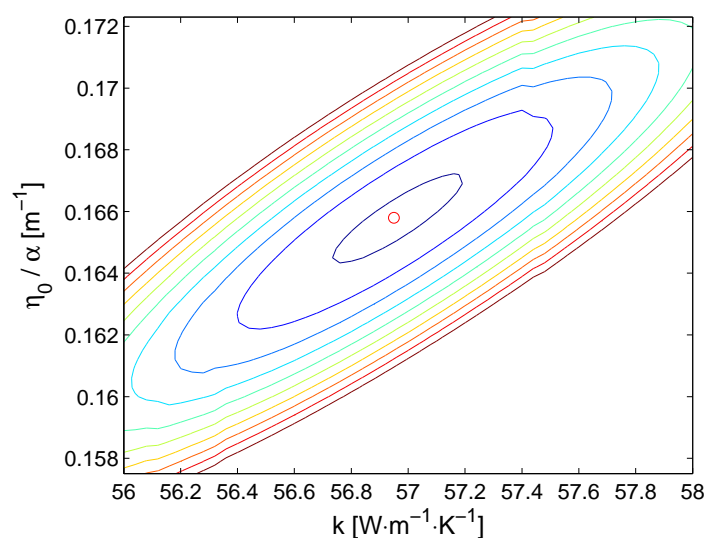

FIGURE 2.14 The equal-value contour lines of the cost function, Eq. (2.25), for the transient temperature profiles of Fig. 2.12. The minimum of the function is indicated by a small circle. The value of the cost function on the innermost contour line is 1 % larger than the minimum value, and subsequent contour lines are drawn at 5-%-unit increments in the value.

The fitted results for all transient-measurement parameters are shown in Table 2.5. According to our measurements, the thermal conductivity of tantalum is $k = (57.5 \pm 0.2) \text{ W} \cdot \text{m}^{-1} \cdot \text{K}^{-1}$, which is in excellent agreement with the generally accepted value in the literature, $57.5 \text{ W} \cdot \text{m}^{-1} \cdot \text{K}^{-1}$, while its thermal diffusivity is $\alpha = (24.74 \pm 0.08) \times 10^{-6} \text{ m}^2 \cdot \text{s}^{-1}$. The parameter $\eta_0/\alpha = (0.158 \pm 0.003) \text{ m}^{-1}$ was 31 % greater than the value obtained from the stationary measurements. This difference can be explained by the different thicknesses of the plates. The transient measurements were done on a factor-of-five times thicker sample than the stationary measurements. Sample thickness can affect the effective heat-loss coefficient η only through the contribution of convective heat transfer. The structure of the flow field of air on both sides of the plate thus seems to depend on sample thickness, causing a thickness dependence also in the convective heat-transfer coefficient.

TABLE 2.5 Fitted parameter values for the transient measurements on the 1.5 mm thick tantalum sample. The values for thermal diffusivity α are related to those of thermal conductivity k by using known values for the density and specific heat of tantalum (Table 2.3). The measured air flow temperatures are also tabulated.

Measurement	k $(\mathrm{W \cdot m^{-1} \cdot K^{-1}})$	α $(10^{-6}\ \mathrm{m^2 \cdot s^{-1}})$	η_0/α $(\mathrm{m^{-1}})$	T_∞ (K)
1	57.6	24.78	0.1469	298.2
2	57.8	24.87	0.1621	297.8
3	57.0	24.53	0.1565	298.0
4	57.7	24.83	0.1593	298.3
5	57.9	24.91	0.1559	298.2
6	57.0	24.53	0.1658	298.3
Average	57.5	24.74	0.1578	298.1

Chapter 3

Thermal diffusivity measurements in a vacuum chamber

The mathematical models for the experimental setup and its improvement introduced in the previous section took into account both radiative and convective heat losses from the sample. However, the radiative heat-loss term had to be linearized in order to combine the two heat-loss components. If we could totally suppress the convective heat transfer, it would enable us to solve (numerically) the corresponding heat diffusion equation without first linearizing the radiative heat-loss term, i.e., the Stefan–Boltzmann law. This would presumably further improve the accuracy of the method and its suitability for poor heat conductors.

3.1   Experimental setup

In order to entirely get rid of the convective heat transfer from the sample we redesigned the experimental setup and placed the sample in a vacuum chamber. In other respects the basic idea of the measurement was the same. The only heat loss mechanism left now was the radiation exchange between the sample and the surroundings. Our stainless steel vacuum chamber was cylindrical with an inner diameter of 0.3 m and a horizontal length of 1.0 m. One end of the chamber could be opened entirely by removing a flange plate. The other end had a smaller flange with an orifice covered by a germanium window 50 mm in diameter and 3 mm thick. The infrared (IR) camera was placed outside the vacuum chamber and the temperature evolution of the sample was recorded through the germanium window. This material was chosen for its good transmittance at infrared wavelengths. The window was installed at an angle of 15 degrees relative to the IR camera lens in order to avoid reflections from the liquid-nitrogen-cooled detector of the camera. A Bourdon tube gage was used to measure the pressure in the vacuum chamber. Typically, the pressure was lower than the minimum reading, 10 mbar, of the gage scale, which was sufficient to eliminate the effect of convection. A quick test measurement showed

that at least at a pressure level of 200 mbar the temperature profiles in the sample were clearly asymmetric.

There were two flat bars welded on the inside walls of the chamber on which there was placed a gliding steel frame. The sample holder was attached to the frame (see Fig. 3.1). With this arrangement it was easy to keep the position of the sample constant during repeated measurements, even if the sample had to be taken out of the chamber in between. The sample holder was made of two split pieces of Bakelite (see Fig. 3.2). One half of both pieces was attached to the steel frame. The sample was pressed between the two halves which were screwed together. The material of the sample holder was chosen based on poor thermal conductivity so as to minimize the conductive heat loss from the sample to the holder.
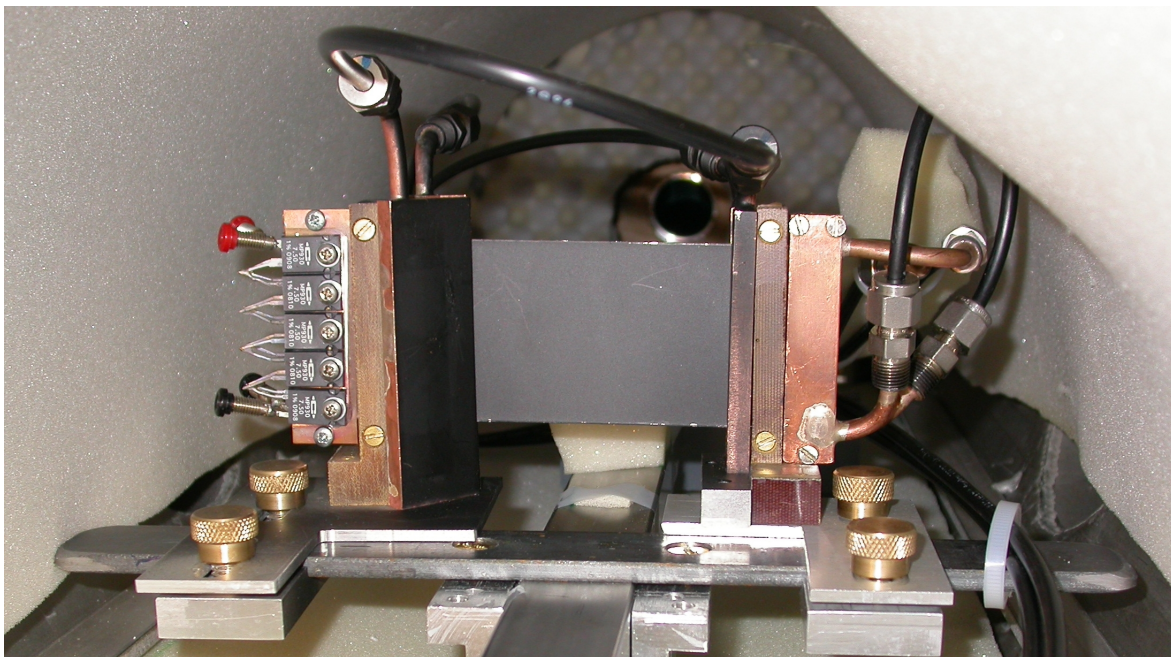

FIGURE 3.1 A planar sample inside a vacuum chamber covered with foamed plastic. On the inside of the units at both ends of the sample are first the room-temperature water-circulation elements and then the sample holders. The outer parts of these units are (left) the heater and cooling (right) elements.

The heater element was separated from the sample holder and consisted of two small copper plates that both had five 7.5-ohm resistors attached side by side to their outer surfaces. The resistors were connected in two series of five resistors and these were then connected in parallel for uniform heating result. The copper plates were tightened around one end of the sample.

At first there was only one sample holder near the heating edge of the sample and the other end was freely in vacuum. It soon turned out that the temperature difference between the two ends was not large enough for accurate determination of thermal conductivity from the temperature profile of the sample. The heat loss from
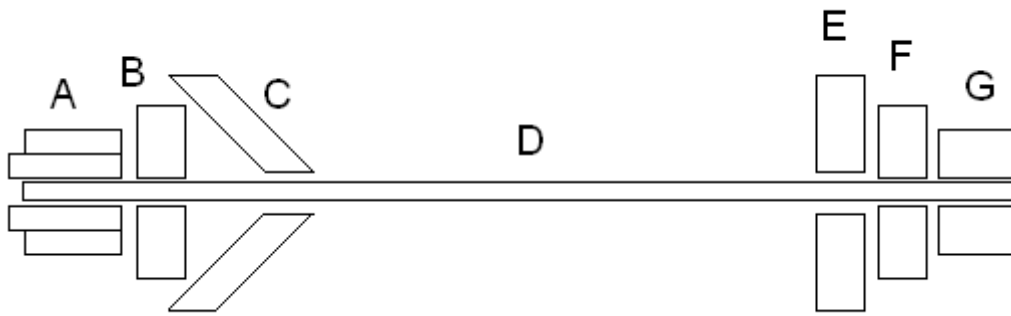
FIGURE 3.2 A cross-section diagram of the experimental setup of Fig. 3.1 as seen from above. A is the heater, B and F are the sample holders, C and E the room-temperature water-circulation elements, D is the sample, and G the cooling element.

the sample by radiation only was too weak for producing a large enough temperature gradient in the sample. To improve the sensitivity of the measurement setup we introduced a water cooling system at the edge opposite to the heated edge of the sample. By this way the temperature difference between the sample edges was enhanced. The free end of the sample was pressed between two halves of a cooling element that consisted of two hollow copper bars inside which cooling water was running.

It became clear that the walls of the vacuum chamber reflected infrared radiation and this affected the measured temperature profile of the sample plate. These complicated reflections would be difficult to handle mathematically. The preferred situation would be the one where the vacuum chamber could be assumed to be a black (or gray) body which means, among other things, diffusive reflections and uniform temperature throughout the chamber. The curved side walls of the vacuum chamber were thus covered with 20-mm-thick foamed plastic and the straight end walls with 50-mm-thick profiled foamed plastic so as to absorb reflections of infrared waves originating from the heater, cooling element, and sample. A thermocouple was attached to each of the thick foamed plastic pieces for temperature measurement of the environment.

There was still a problem that caused artifacts in the temperature profile. The sample holder warmed up during the heating of the sample and consequently there was radiative heat transfer between the two. Also, at the other end of the sample the cold cooling element absorbed heat from the sample. In order to prevent the sample from directly 'seeing' the warm end of the sample holder warmed up by the heater element, or the cold end cooled down by the cooling element, a water-cooled shielding element was added to the system. Water at room temperature was circulated through two hollow copper plates attached to each end of the sample holder. In this way the whole surroundings seen by the sample was kept at uniform temperature, i.e., that of the vacuum-chamber walls.

The samples were painted thinly on both sides with black spray paint for enhanced sample emittance and thereby for better visibility to and sensitivity of the IR camera. The IR camera was calibrated for each sample against a thermocouple that was sandwiched between the back side of the sample and a same-size copper plate. The temperature at that point of the sample was measured with the IR camera. During calibration the sample temperature was controlled and kept constant by two heaters, one at each end of the sample. The thermocouple was located in the middle of the sample between the heaters, where temperature gradient was zero.

3.2   Mathematical model

As there was no convection present in our experimental setup, the temperature field in the sample was symmetrical with respect to its center line, as was the case in the earlier setup for very good conductors of heat (section 2.3). We thus restricted our consideration again to a narrow strip at the center line of the sample plate and used a one-dimensional heat equation to describe the system,

$$\rho \, c_p \, \frac{\partial T}{\partial t} = k \, \frac{\partial^2 T}{\partial x^2} - \frac{2}{a} \, \epsilon_s \, \sigma \, (T^4 - \epsilon_c T_c^4). \tag{3.1}$$

The nomenclature is the same as before with a couple of new parameters. Sample emissivity, ϵ_s, and the emissivity of the chamber walls, ϵ_c, are assumed to be constants. T_c is the temperature of the chamber walls. In Eq. (3.1) it has been assumed that the absorptivity of the sample is equal to its emissivity, and that the thermal conductivity k is constant and does not depend on temperature.

One end of the sample plate was heated and the time dependence of its temperature $T(0, t)$ was measured. The opposite end was cooled to keep the temperature there as constant as possible, but the time evolution of this temperature, $T(L, t)$, was also measured. So, the initial and boundary conditions for Eq. (3.1) are

$$\begin{cases} T(x, 0) = f(x), \\ T(0, t) = T_0(t), \\ T(L, t) = T_L(t), \end{cases} \tag{3.2}$$

where L is the length of the plate. The initial temperature distribution $f(x)$ and the temperatures $T_0(t)$ and $T_L(t)$ were obtained from the IR-camera measurements.

To determine the unknown emissivity of the measurement chamber, ϵ_c in Eq. (3.1), we made some transient temperature measurements with a tantalum sample. Tantalum was chosen because its thermal conductivity remains constant over the temperature range that was used in our measurements. Temperature-dependent thermal properties would have complicated accurate determination of the emissivity of the vacuum chamber. The thermal properties of Ta were known (see Table 2.3),

and the two remaining unknown parameters were determined from the measurements by minimizing the cost function

$$\int_{x_1}^{x_2} \left(\int_{t_1}^{t_2} \left(T_{(\epsilon_c,\,\epsilon_s)}(x,t) - \bar{T}(x,t) \right)^2 \, \mathrm{d}t \right) \mathrm{d}x \tag{3.3}$$

with respect to ϵ_c and ϵ_s. Here $T_{(\epsilon_c,\,\epsilon_s)}$ is the numerical solution of the boundary value problem, Eq. (3.1) with Eq. (3.2), and $\bar{T}$ is the measured transient temperature profile, averaged over the central fifth of the sample.

For the other samples (stainless steel and low-carbon steel) that were studied to validate the method, the measured transient temperature data were fitted similarly as for tantalum, but the two unknown parameters were now the thermal conductivity, k, and the emissivity, ϵ_s, of the sample.

3.3 Validation of the method

A 0.25-mm-thick tantalum sample was used for the determination of chamber emittance. One end of the sample was first cooled down and, after reaching a steady-state condition, the heater at the other end was switched on. The time evolution of the temperature field in the sample was recorded by the IR camera connected to a PC. One image per second was saved during the heating, because now the temperature rise in the sample was quite slow. The images were averaged over the central fifth of the sample width so as to obtain a one-dimensional time-dependent mean temperature profile. An example of (part of) the measurement data is shown in Fig. 3.3.

Numerical solution to Eq. (3.1) with Eq. (3.2) was computed for several values of the fitting parameters, ϵ_c and ϵ_s, using the material properties of tantalum at 300 K given in Table 2.3. The fitted results for all measurements are given in Table 3.1, and contours of the cost function, Eq. (3.3), for the first measurement are shown in Fig. 3.4. The normalized cost-function values I_{norm} in Table 3.1 were obtained by dividing the minimum of the cost function by the integration area. This normalization was done so that comparison between individual measurements would be reasonable. According to our measurements, the emittance of the vacuum chamber was $\epsilon_c = 0.950 \pm 0.002$, and this value was used later when fitting other measurement data (two steel samples). The emittance of the tantalum sample plate was found to be $\epsilon_s = 0.961 \pm 0.011$.

A 0.5-mm-thick low-carbon steel sample that consisted mostly of iron (about 99.2 %) was measured to check that the method and equipment worked properly. Measurement data for this case are shown in Fig. 3.5 together with the best fit. Contour lines of the cost function, Eq. (3.3), with fitting parameters k and ϵ_s, are shown in Fig. 3.6. The results for all measurements are given in Table 3.3, and they indicate that the thermal conductivity of the sample was $54.8 \pm 0.6 \; \mathrm{W \cdot m^{-1} \cdot K^{-1}}$. This is
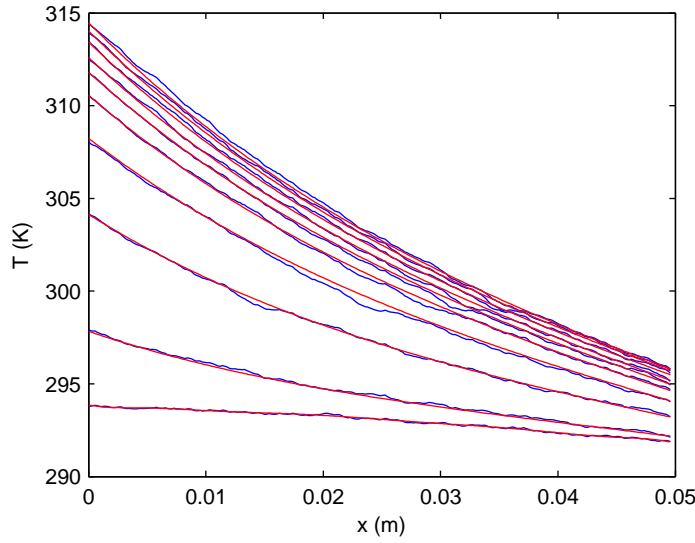
FIGURE 3.3 Transient temperature profiles in a 0.25-mm-thick tantalum sample at 60 s intervals (blue) together with the best fit (red) by the model, Eqs (3.1) and (3.2).

TABLE 3.1 The values of best-fit parameters for the individual measurements on the tantalum sample. I_{norm} is the normalized value of the cost-function minimum. Error estimates are based on the standard deviation of the mean.

Measurement	ϵ_c	ϵ_s	I_{norm} (K^2)
1	0.956	0.93	0.016869
2	0.950	0.99	0.010438
3	0.945	0.95	0.016143
4	0.945	0.98	0.012299
5	0.954	0.97	0.011550
6	0.943	0.99	0.016001
7	0.954	0.92	0.019381
Average	0.950	0.961	0.0147
Error estimate	0.002	0.011	0.0013

TABLE 3.2 Density, specific heat, and heat conductivity of the sample materials at 300 K.

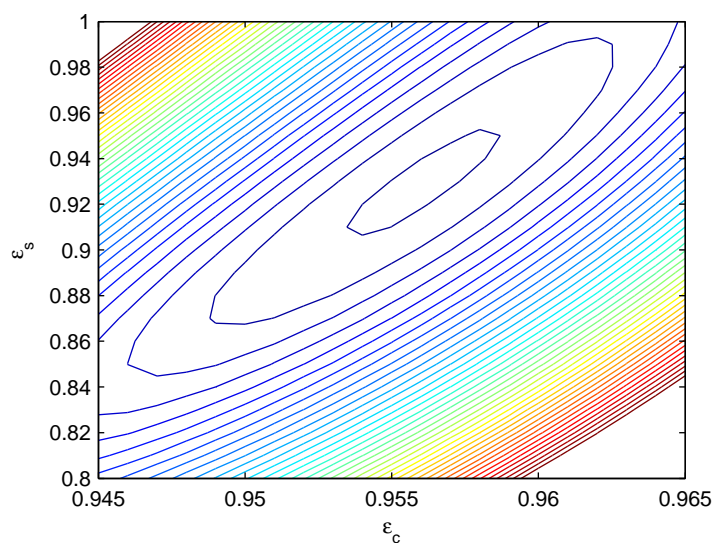| Sample	ρ $(kg \cdot m^{-3})$	c_p $(J \cdot kg^{-1} \cdot K^{-1})$	k $(W \cdot m^{-1} \cdot K^{-1})$
stainless steel	7900	440	15.0
low-carbon steel	7870	447	62
bronze	8780	355	54

FIGURE 3.4 Contour lines of the cost function, Eq. (3.3), for a tantalum measurement. The best fit for the measured temperature data is provided by parameter values $\epsilon_c = 0.956$ and $\epsilon_s = 0.93$ which minimize the cost function. Each contour line indicates a 5 % increase in the cost-function value compared to its minimum value.

about 12 % lower than the value quoted in Table 3.2, which was obtained from the manufacturer and was estimated based on the material composition.

As another verification, we made measurements on a 0.8-mm-thick stainless steel sample. The resulting best-fit parameters are given in Table 3.4. The thermal conductivity was found to be in this case $14.33 \pm 0.09 \ \text{W} \cdot \text{m}^{-1} \cdot \text{K}^{-1}$, which is slightly (by less than 5 %) lower than the value $15.0 \ \text{W} \cdot \text{m}^{-1} \cdot \text{K}^{-1}$ provided by the manufacturer. The mean value of the emissivity of the sample was 1.01, which is of course unphysical, but fluctuations between the individual measurements in this parameter were about ten times larger than those in the thermal conductivity, and evidently the number of the measurements did not provide a representative value for this quantity. As the thermal conductivity did not seem to depend too much on sample emissivity, measurements were not continued.
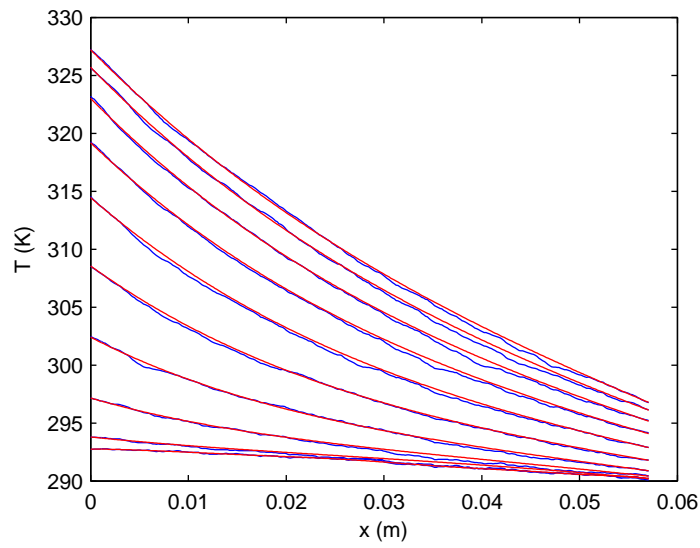
FIGURE 3.5 Transient temperature profiles in a 0.5-mm-thick low-carbon-steel sample at 30 s intervals (blue) together with the best fit by the model (red).
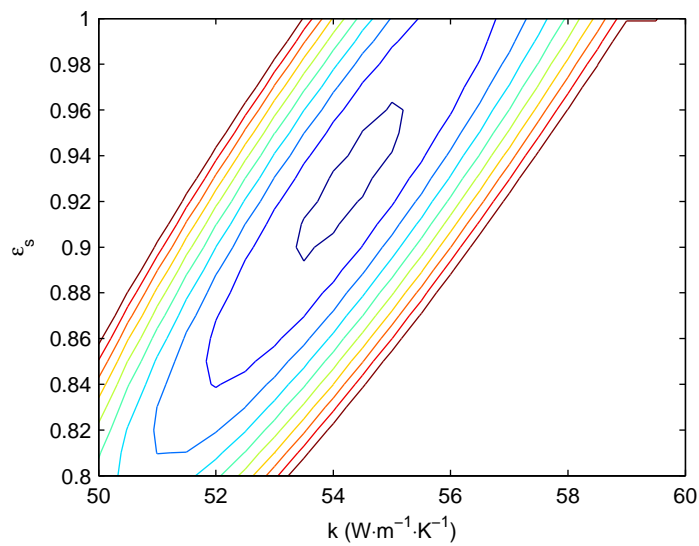

FIGURE 3.6 Contour lines of the cost function, Eq. (3.3), for a measurement on the low-carbon-steel sample. The innermost contour line shows the 1 % difference to the minimum of the cost function value and thereafter each line indicates an additional 5-%-unit increase in the value.

TABLE 3.3 The values of best-fit parameters for the individual measurements on the low-carbon-steel sample.

Measurement	k (W$\cdot$m$^{-1}\cdot$K^{-1})	ϵ_s	I_{norm} (K^2)
1	54.5	0.95	0.017431
2	52.5	0.83	0.031479
3	57.0	1.07	0.017849
4	54.0	0.91	0.017667
5	54.0	0.98	0.017464
6	56.0	1.07	0.017593
7	54.0	0.92	0.020850
8	56.5	1.05	0.016896
Average	54.8	0.97	0.021
Error estimate	0.6	0.04	0.003

TABLE 3.4 The values of best-fit parameters for the individual measurements on the stainless-steel sample.

Measurement	k (W$\cdot$m$^{-1}\cdot$K^{-1})	ϵ_s	I_{norm} (K^2)
1	14.5	0.97	0.017434
2	14.1	0.90	0.005049
3	14.4	1.15	0.008680
4	14.3	1.03	0.008169
Average	14.33	1.01	0.010
Error estimate	0.09	0.06	0.003

Chapter 4

Effective thermal conductivity of porous materials

Porous materials are used in many applications, e.g., as insulators, filters and separators, and knowledge of the heat transport properties of the substance is often important. The thermal conductivity of such a material may differ greatly from that of solid 'bulk' material of which the porous material is made. Inside the material there is air or some other fluid (or even vacuum in some cases) surrounding solid particles that form the 'skeleton' of the material. Heat transport in this kind of complex network of solid and fluid phases is a complicated process and involves all three heat transport modes. However, the heat transfer rate through the material can be described by an effective thermal conductivity, i.e., the thermal conductivity the sample would have if it was regarded as a block of homogeneous material.

The effective thermal conductivity of porous materials is not only dependent on the properties of the solid component and porosity, but also the structural organization of the material plays an important role. That is it depends on the way the solid constituents of the material are connected so as to form a three-dimensional (3D) body [18].

A common group of porous materials is formed by packed beds of solid (mostly spherical) particles. Especially packed beds with regular structures have been much studied analytically, and many results for their effective thermal conductivity are given in Ref. [19, pp. 129-130], see also [20]. It is important to determine how well the analytical (averaged) expressions describe the properties of real porous materials. This question is in essence related to how the relevant structural parameters used in theoretical expressions can actually be determined except for regular structures. Recently methods of X-ray tomography have been advanced so that such questions can now be answered via 3D structural analysis. To begin with one has, however, to measure the effective thermal conductivity. The method for measuring thermal conductivities in vacuum as described in the preceding chapter is well suited for porous samples, as long as their thermal diffusivity is high enough.

4.1 Theoretical expectations

For the porous material, filters made of sintered bronze spheres was chosen, also because a similar problem had been investigated theoretically by Chan and Tien [21], who had studied thermal conductivity of packed spheres in vacuum. Their spheres were of uniform size and the contacts between spheres were assumed to follow the Herzian elastic deformation relation,

$$R_c = \left[\frac{3(1 - \mu_p^2)}{4E_s}FR\right]^{1/3}, \ R_c \ll R, \tag{4.1}$$

where R_c is the radius of the spherical contact area, μ_p the Poisson ratio of the material, E_s its Young's modulus, and F the force pressing the spheres of radius R together. They assumed a uniform heat flux through the contact surface and calculated the thermal resistance of a single sphere. Thermal resistance can be defined as the ratio of the temperature difference between two opposing contacts of the sphere to the conductive heat flux through the sphere.

The thermal resistance of a system consisting of packed spheres was considered in Ref. [21] as a network of individual thermal resistances, and the final outcome depended on the structure of the packing. Results were given for simple cubic, body-centered cubic, and face-centered cubic lattices. The ratio of the effective thermal conductivity, k_e, of the porous material to the conductivity of the solid sphere material, k_s, was found to be given by [19, p. 132]

$$\frac{k_e}{k_s} = \left[\frac{3(1 - \mu_p^2)}{4E_s}FR\right]^{1/3} \cdot \frac{1}{0.531S}\left(\frac{N_A}{N_L}\right), \tag{4.2}$$

where N_A is the number of particles per unit area in the plane perpendicular to the heat flow and N_L is the number of particles per unit length along the direction of the heat flow. The value of constant S depends on the packing structure such that S^{-1} gives the number of contact pairs through which heat flows into and out of an individual sphere. In the case of irregular packings, S^{-1} can be considered as the average number of such contact pairs per particle.

It is evident from Eqs (4.1) and (4.2) that the effective thermal conductivity of a porous material is proportional to the size of the total contact area, $2\,R_c/S$, for an individual particle. So as to test such dependences we imaged the porous samples with X-ray tomography, and determined the quantities that appear in Eq. (4.2) from the resulting 3D images. Furthermore, these tomographic images were used to simulate heat diffusion (conduction) through the system of solid particles. In these simulations we could also include, if necessary, the effect of contact resistance that is missing from Eq. (4.2), and thereby analyze its importance in real materials.

4.2 Thermal conductivity of sintered bronze plates of varying porosity

The measurement method developed and validated as described in Chapter 3 was applied to three samples made of sintered bronze (89 % Cu + 11 % Sn) by GKN Sinter Metals Filters GmbH. The relevant properties of these samples are given in Table 4.1. Properties of bulk bronze were already given in Table 3.2. The porosities of the samples were obtained from X-ray tomographic images described in the next section. An example of contour lines of the cost function, Eq. (3.3), with fitting parameters k and ϵ_s, are shown in Fig. 4.1 for a measurement on sample B 30. The averaged results for the measured thermal conductivities of the three samples are given in Table 4.2. These effective thermal conductivities are roughly 20 % of the conductivity value $54\,\mathrm{W \cdot m^{-1} \cdot K^{-1}}$ for bulk bronze.

TABLE 4.1 Porosity, thickness, and density of the samples made of sintered bronze.

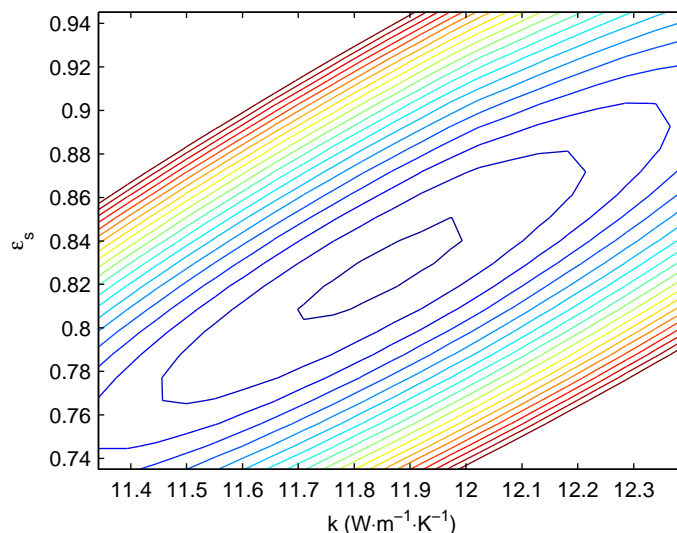| Sample	ϕ (%)	thickness (mm)	$\rho\,(\mathrm{kg \cdot m^{-3}})$
B 30	37 ± 1	2.00 ± 0.05	5650 ± 150
B 45	38 ± 2	2.05 ± 0.05	5420 ± 140
B 80	42 ± 2	1.80 ± 0.05	5260 ± 150

FIGURE 4.1 Contour lines of the cost function for a sintered bronze plate (sample B 30) measurement. The best fit for the measured temperature data is provided by parameter values $k = 11.87\,\mathrm{W \cdot m^{-1} \cdot K^{-1}}$ and $\epsilon_s = 0.83$ which minimize the cost function. The value of the cost function on the innermost contour line is 1 % larger than the minimum value, and thereafter each line indicates an additional 5-%-unit increase in the cost-function value.

TABLE 4.2 The average values of the best-fit parameters for the measurements on the sintered bronze plates.

Sample	k $(\mathrm{W \cdot m^{-1} \cdot K^{-1}})$	ϵ_s	I_{norm} (K^2)
B 30	12.0 ± 0.3	0.85 ± 0.06	0.017 ± 0.003
B 45	9.68 ± 0.08	0.84 ± 0.04	0.0193 ± 0.0010
B 80	9.3 ± 0.2	1.04 ± 0.02	0.0101 ± 0.0008

Because the measurement setup was in vacuum, the measured thermal conductivities for porous materials are lower limits. In air the conductivity should be slightly higher as the pores are then filled with air, although it is a poor conductor of heat.

The emissivity of sample B 80 deviates from those of the other two samples, and the result is unphysical. Even with the lower error limit the result is greater than one. In Chapter 3.3 the measured emissivity of the 0.8-mm-thick stainless steel sample was 1.01 ± 0.06, which was explained by large fluctuations between four individual measurements. Experimental data for sample B 80 consist of seven measurements and, as evidenced by the small error limits, fluctuations between individual measurements were quite low. The fits to the measured temperature profiles were also good, because of the three sintered bronze samples the cost function value I_{norm} was the lowest for B 80 (see Table 4.2). The only explanation left for the too large emissivity is that, in addition to radiative heat transfer, there has been another mechanism of heat transfer from the sample. Most probably some heat from the sample has escaped by conduction through connections with the sample holders (see Fig. 3.2), and this is seen as an abnormally high apparent emissivity. This phenomenon is most significant for samples that are poor heat conductors.

4.3 3D structural analysis of sintered plates by X-ray tomography

X-ray tomography is a method for obtaining a 3D digital representation of the inner structure of a sample based on differences in the attenuation of X-rays inside the sample. The method is based on computational reconstruction of a series of 2D X-ray projection images into a 3D representation. The projection images are obtained by exposing the sample to X-rays from various angles by rotating the sample around its axis on a sample holder. Typically a 180- or 360-degree rotation is used with a step size of less than one degree. The X-ray source is an X-ray tube in table-top scanners. The detector is a 2D CCD chip coupled with a scintillator plate that converts sample-penetrating X-rays into visible light.

The end product of an X-ray tomography scan and reconstruction procedure is a 3D data matrix that contains the X-ray attenuation factors (proportional to ma-

terial density) in the volume of view of the CT scanner. In other words the device generates a 3D density map of the sample and air that are in the scanning area. This density map can be considered as a 3D image of the sample structure and can be analyzed and used in simulations. X-ray tomography thus enables one to analyze samples with their original complex structure without destroying or mechanically altering their structure during imaging.

The sintered bronze plates were imaged with an X-ray microtomography scanner (Xradia MicroXCT-400) for detailed 3D reconstructions of their structure. The voxel sizes of the images were $(1.95 \ \mu\text{m})^3$, $(3.03 \ \mu\text{m})^3$, and $(3.13 \ \mu\text{m})^3$ for the samples B 30, B 45, and B 80. A part of sample B 30 is visualized in Fig. 4.2.
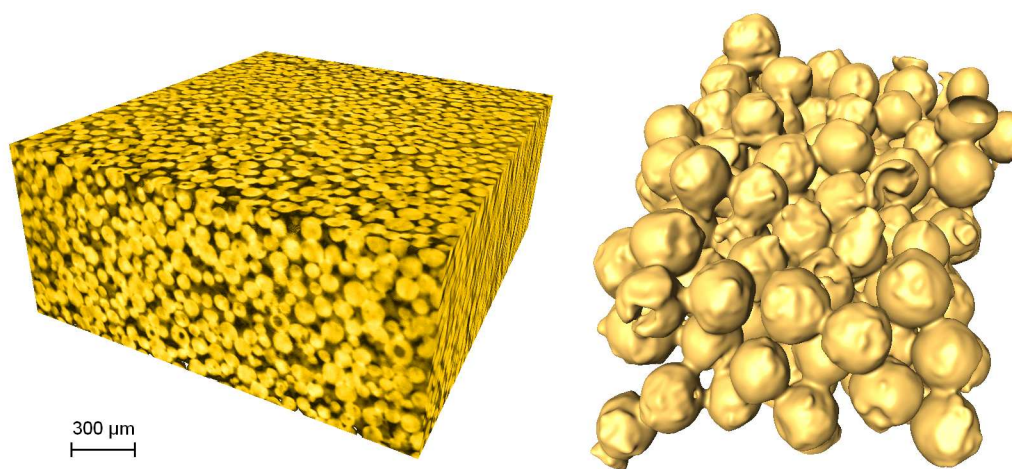

FIGURE 4.2 A 3D visualization of part of a tomographic reconstruction of sample B 30 (left) and a zoomed-in 3D rendering of some particles inside the sample (right). The average diameter of the particles was about $130 \ \mu$m. Figures: Tuomas Turpeinen.

For quantitative structural analysis the original gray-scale images of the samples were first thresholded so that bronze and air were segmented from each other, see Figs 4.3 (a) and (b). The porosity of the sample was then easily determined by dividing the number of black voxels (now representing void volume) by the total number of voxels. Next the thresholded black and white images were further segmented so as to identify the individual spherical bronze particles for more detailed structure analysis. To find the particle boundaries a watershed segmentation algorithm [22] was applied. This was the most challenging part in the structural analysis. Algorithmic software development was needed to complete this task. An example of a sample with segmented particles is shown in Fig. 4.3 (c). For each identified particle we determined the volume, surface area, and number and area of contacts ('throats') with neighboring particles. From these results the particle-size and contact-area distributions were computed.

It was also possible to compute the number of particles per unit area and per unit length of the sample, the quantities N_A and N_L, respectively, of Eq. (4.2). But first it was necessary to determine the volume in which to count the particles. One

side in every sample was quite even, but the other one was rough. On the rough surface the particle density was lower than in the bulk material. If a sample had been cropped according to the highest peaks of the two surfaces, a lot of air would have been included and thus the particle densities would have become unrealistically low. Instead, mode heights of the two surfaces were used as boundaries. The particle number distributions are shown for sample B 45 in Fig. 4.4. Notice that these distributions were plotted for pure number of particles counted for a certain cross-section area and sample length, and thus the (dimensionless) distributions are denoted by N_A^* and N_L^*. The distributions N_A and N_L were obtained by dividing N_A^* and N_L^* by sample area and length, respectively.

Mode surface heights were, however, not used when determining the thickness of a sample, because they would have led to a too low thickness value. The rough surfaces were instead identified by fitting them with a flexible, elastic, falling sheet. By an appropriate choice for the value of a stiffness parameter, the relaxed sheet followed the surface shapes close enough, but still smoothing them sufficiently. Mean thickness was then calculated for the volume constrained by elastic surfaces on both sides.
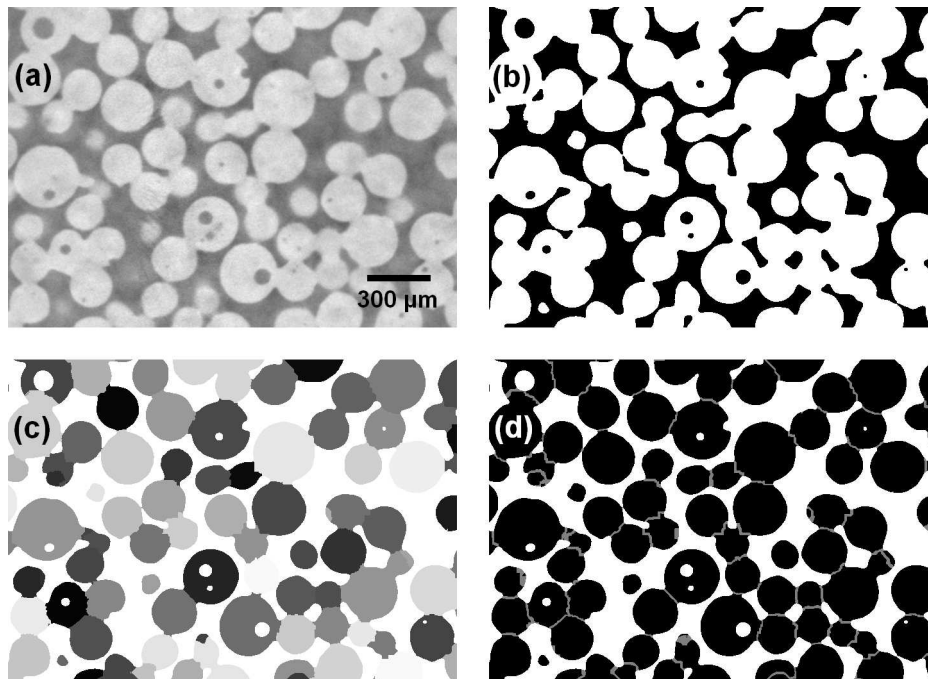

FIGURE 4.3 (a) A thin slice of an X-ray tomographic reconstruction of sample B 45. (b) A thresholded version of (a) in which bronze (white) and air (black) have been segmented. (c) The result of segmentation of the individual particles by applying a watershed algorithm. Individual bronze particles are marked by random gray-scale values. (d) The contacts between segmented particles are highlighted with 2-voxel-thick gray boundaries.

Another important quantity was the total contact area for each bronze particle,
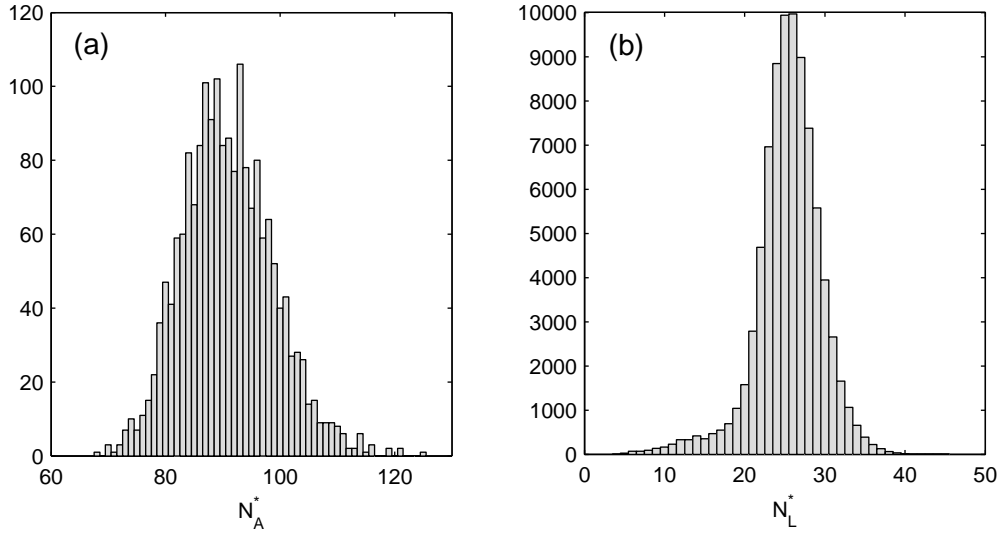
FIGURE 4.4 (a) Distribution of the number of bronze particles per an area of 660 × 500 pixels for sample B 45. The mean of the distribution is 90.9. (b) Distribution of the number of particles per sample length of 1857 pixels with a mean value of 25.5. The pixel size in this sample was 3.03 μm.

which is needed for obtaining an estimate for the parameter R_c/S that also appears in Eq. (4.2). The distribution of the total contact area per particle is shown in Fig. 4.5. The mean values of the distributions determined for the three samples are given in Table 4.3.

TABLE 4.3 The mean values of the distributions determined by X-ray tomography and image analysis for the sintered bronze plates.

Sample	N_A (10^6 m^{-2})	N_L (10^3 m^{-1})	$A_{contact}^{tot}$ (10^{-8} m^2)
B 30	90.8	7.50	2.535
B 45	30.1	4.53	5.773
B 80	13.2	2.90	10.156

We are now in the position to check the validity of Eq. (4.2) in the form

$$\frac{k_e}{k_s} = \frac{1}{0.531}\frac{R_c}{S}\frac{N_A}{N_L} \propto \sqrt{\frac{A_{contact}^{tot}}{\pi}}\frac{N_A}{N_L}, \tag{4.3}$$

which is now directly related to quantities determined by X-ray tomography analysis. The left-hand side of this equation is the ratio of measured thermal conductivity to that of bulk bronze given in Table 3.2. The result, k_e/k_s as a function of $(A_{contact}^{tot}/\pi)^{1/2} \cdot N_A/N_L$, is plotted in Fig. 4.6.

It is evident from Fig. 4.6 that the measured thermal conductivities for sintered bronze plates follow roughly the dependence suggested by Eq. (4.3). The biggest
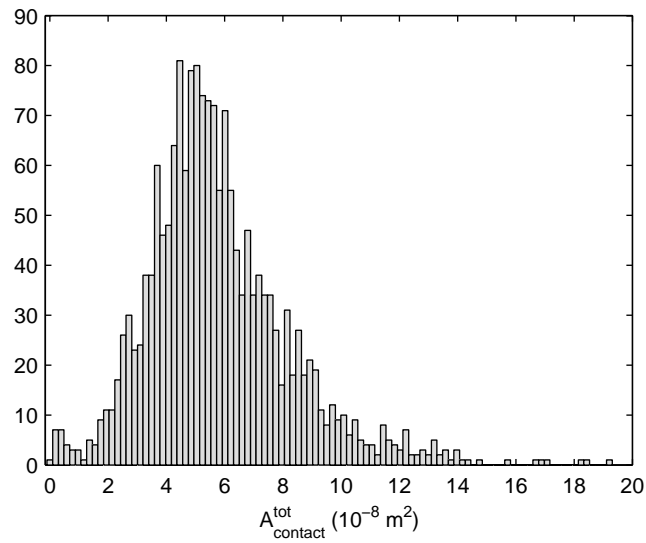
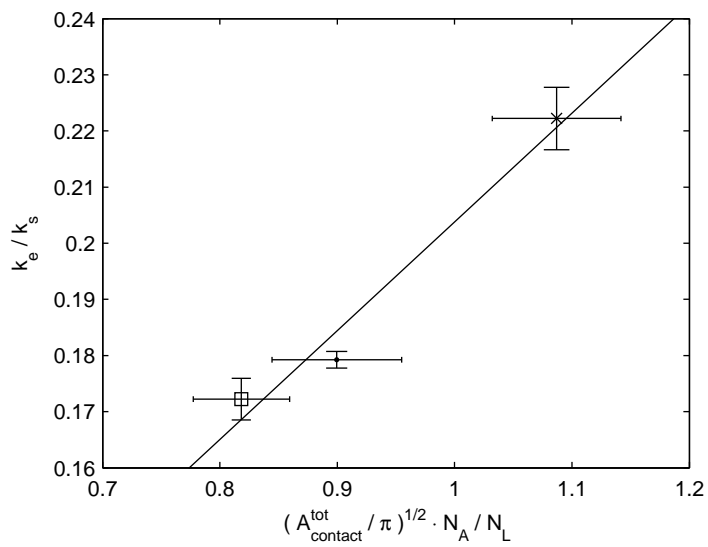**FIGURE 4.5** Distribution of the total contact area per particle for sample B 45.

FIGURE 4.6 The measurement data as a function of $(A^{tot}_{contact}/\pi)^{1/2} \cdot N_A/N_L$ for the three sintered bronze plates. The samples corresponding to the data points from top to bottom are B 30 ($\times$), B 45 ($\cdot$), and B 80 ($\square$).

uncertainty lies in the x coordinates of the measurement data in Fig. 4.6 because of the wide distributions of the total contact area and the number of particles per unit area and length. In order to analyze the thermal conductivity in the samples in more detail, numerical heat-conduction simulations in tomographic reconstructions of the sintered plates were performed.

4.4 Simulation of thermal conductivity in tomographic reconstructions of sintered plates

Segmented X-ray tomography images were used as simulation geometries in a numerical determination of the thermal conductivity of the sintered bronze plates. For these simulations the final segmented images were manipulated so that to each contact a two-voxel-deep layer was added, and the rest of the particles were treated as bulk bronze, see Fig. 4.3 (d). In this way it was possible to associate the contacts with a different (smaller) thermal conductivity than that of bronze so as to incorporate the effect of thermal (contact) resistance between individual particles. Simulations were based on the lattice-Boltzmann method [23] that has recently been applied successfully to porous structures [3, 24].

The lattice-Boltzmann (LB) method is a kinetic-theory-based mesoscopic approach used to simulate various transport phenomena. Most commonly, the LB method has been used to simulate fluid flow, but it also suits well to, e.g., mass and heat diffusion problems. One of the main advantages of the LB method is the straightforward implementation of boundary conditions, which enables simulations in complex geometries such as porous materials. Thus, we can directly use the segmented tomographic reconstructions as the computational lattices and solve the heat-conduction problem in the imaged structures.

For practical reasons, the tomographic images were divided into three smaller pieces in the direction of the heat flow in the experiments. In each piece a constant temperature was imposed at two opposite edges of the sample, and the conductive heat transfer through the sample was simulated until a steady state was obtained. The steady-state heat flux was determined, and the effective thermal conductivity was obtained from that.

For each sample thermal conductivity was simulated first without contact resistance between contacting particles. Results from the simulations are shown in Table 4.4 together with the measured thermal-conductivity ratios. The simulation result for each sample was taken as the average of the results for the three smaller geometries. Thermal conductivities between the smaller pieces varied a couple of percent.

The simulated thermal-conductivity ratios were systematically higher than the measured ones. A possible explanation to this discrepancy lies in the resolution of

TABLE 4.4 Ratio of the effective thermal conductivity to bulk bronze conductivity for the sintered bronze samples. Simulations by the lattice-Boltzmann method are compared to measurements.

Sample	Measured k_e/k_s	Simulated k_e/k_s	Difference (%)
B 30	0.222 ± 0.006	0.286	29
B 45	0.179 ± 0.002	0.279	56
B 80	0.172 ± 0.004	0.252	46

the X-ray tomographic images. Simulations are sensitive to the throat areas between bronze particles, and these contacts were determined from the segmented X-ray reconstructions. If resolution is not good enough, small gaps between adjacent particles may appear as closed, and the contact area is increased from its true value, which leads to a higher effective thermal conductivity in the simulations.
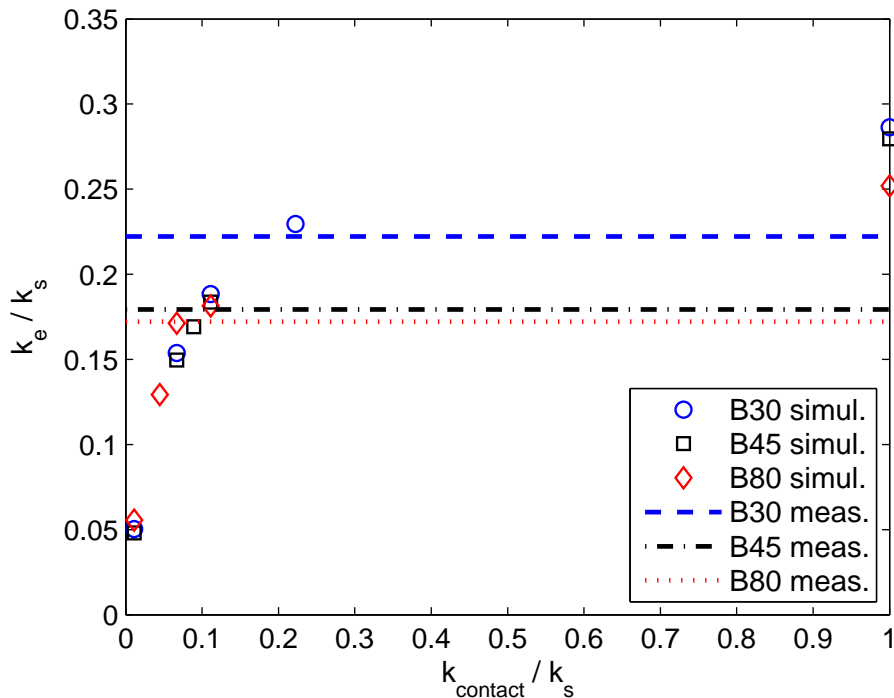

FIGURE 4.7 The effect of contact resistance between bronze particles on the effective thermal conductivity of the sample by lattice-Boltzmann simulations. The measured effective-to-bulk thermal-conductivity ratios are indicated by the horizontal lines. Simulation data by Jari Hyväluoma.

For each sample thermal conductivity was also simulated for a varying contact resistance between contacting particles, assumed to be the same for all the contacts in a given sample. The resulting simulation data (see Fig. 4.7) indicated a progressively lower thermal-conductivity ratio k_e/k_s for all samples as the thermal contact resistance was increased, i.e., the thermal conductivity of the contacts was de-

creased. Matching simulation data with the measurement results also proposed that the contact resistance would be different for each sample. The smallest contact resistance, i.e., the largest $k_{contact}/k_s$ ratio was determined for sample B 30 that was imaged with the smallest voxel size, $(1.95\ \mu\text{m})^3$. Also, the largest contact resistance was related to sample B 80 that was imaged using the largest voxel size, $(3.13\ \mu\text{m})^3$. This supports the assumption that insufficient resolution has induced an apparent contact resistance.

The effect of contact resistance (whether it is real or apparent, i.e., induced by overestimating the contact areas because of insufficient resolution in the simulation geometries) can be included in the theoretical expression Eq. (4.3). Assuming that the heat conductivity (current) through a contact is proportional to contact area, the latter can be normalized by the real or apparent contact resistance determined by simulations. This means that the total contact area per particle was reduced by a factor of 0.195 in sample B 30, 0.105 in B45, and 0.075 in B80. After this renormalization of $A_{contact}^{tot}$ to $A_{contact}^{ren}$, we find the results shown in Fig. 4.8.
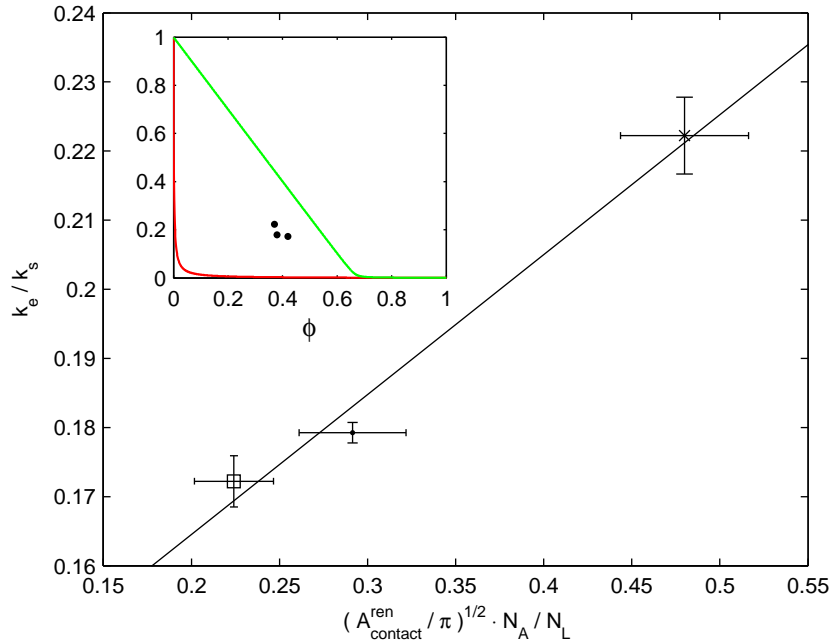

FIGURE 4.8 A linear least-squares fit to the measurement data as a function of $(A_{contact}^{ren}/\pi)^{1/2} \cdot N_A/N_L$ for the three sintered bronze plates. The samples corresponding to the data points from top to bottom are B 30 ($\times$), B 45 ($\cdot$), and B 80 ($\square$). The total contact area per particle was normalized in every sample so as to take into account the overestimation of contact areas in the tomographic images. In the inset the measurement data (dots) are shown as a function of porosity. The lines are theoretical upper (effective-medium theory, green line) and lower (dispersed particles, red line) bounds for the dependence.

Interestingly, the results that include renormalized contact areas look similar

to those of Fig. 4.6. It may have been just a coincidence that the different contact resistances of the samples were such that, after correcting the total contact area per particle, the relative locations of the three data points remained almost the same as before the correction. The inset of Fig. 4.8 shows the measured thermal conductivity ratio as a function of porosity. Theoretical thermal-conductivity bounds given by the Maxwell–Eucken model for dispersed particles (lower bound) [25] and the Effective-Medium Theory (upper bound) [26, 27] for two continuum phases are also plotted for comparison [18]. Even though the particles were not dispersed in the sintered bronze plates, it is evident that the effective conductivity can hardly be described by a simple function of porosity as the area of possible conductivities between the upper and lower bounds is very large. Also, the relative locations of the measured points even for the short range of porosities covered indicate a similar conclusion. It is clear that more than one structural parameter are needed to describe the thermal conductivity of sintered bronze plates.

In conclusion, the theoretical result, Eq. (4.3), explained well the measured thermal conductivities for the present samples, when their detailed 3D structure was analyzed. Notice that three structural parameters are needed to describe the thermal conductivity and that there appears to be no simple relationship between heat conductivity and porosity. The effect of thermal contact resistance, or incorrect contact area, between constituent particles could be included in the model by normalizing the contact areas determined by tomographic analysis. This effect was estimated by numerical simulations based on tomographic reconstructions of the samples. In the present set of samples, there should not have been any significant (real) contact resistance. According to the simulation results the smallest apparent contact resistance, i.e., the largest $k_{contact}/k_s$ ratio, was determined for sample B 30 that was imaged with the smallest voxel size. Also, the largest apparent contact resistance was related to sample B 80 that was imaged using the largest voxel size. This supports the assumption that insufficient resolution in the simulation geometries had induced an apparent contact resistance due to overestimation of the contact area. Tomographic images of samples with a better voxel resolution also supported this assumption as narrow gaps beween particles could be observed, which disappeared when the images were thresholded into bronze particles and air. In principle this effect could be confirmed by numerical simulations of conductivity using tomographic reconstructions of clearly higher resolution. Unfortunately high resolution means small sample size, and such simulations would not give representative results (and would be too time consuming if large sample sizes could somehow be used). In the 3D structural analysis by X-ray tomography, the most challenging task was thus the segmentation of individual particles. Algorithmic software development was needed to reach even the present segmentation results that were estimated to be satisfactory. The contact area between particles is sensitive to image quality, and at present it seems difficult to avoid the narrow-gap problem. Methods

should be developed further, or some other methods should be incorporated as we did here, so as to better estimate this parameter.

Chapter 5

Height-fluctuation distributions of slow-combustion fronts in paper

Slow-combustion fronts in paper sheets have been studied earlier [7]. The sheets were treated with potassium nitrate (KNO_3), because without an oxidizer paper would not burn slowly (flamelessly) for extended periods of time. Then a paper sheet aligned vertically was induced to smolder by igniting it on one edge with an electrically-heated tungsten wire. The time evolution of the smoldering front in paper was recorded with a CCD-camera system for data analysis. The slow-combustion fronts in paper were shown to belong to the KPZ universality class [7], i.e., the dynamics of a propagating front is statistically governed by the Kardar-Parisi-Zhang equation [28] which can be written in the form

$$\frac{\partial h}{\partial t} = \nu \frac{\partial^2 h}{\partial x^2} + \frac{\lambda}{2} \left(\frac{\partial h}{\partial x} \right)^2 + \eta(x, t) \qquad (5.1)$$

for a one-dimensional front in a two-dimensional space. Here $h(x, t)$ is the local position (height) of the propagating front, ν is the surface tension parameter, λ is the coefficient of the nonlinear term, and η is the noise term that is assumed to be Gaussian and uncorrelated. Notice that here we denote the front position by h, while the coefficient of convective heat transfer is denoted by Γ (in contrast with the previous chapters).

Propagation of combustion fronts in paper is essentially a heat transport problem. Combustion is a chemical reaction that produces heat which is then transported away by conduction along the paper and by convection (and radiation) to the surrounding air. The whole propagation process can be studied by a temperature field T in the paper. When the radiative heat transfer is neglected, the evolution of the temperature field is described [8] by the equation

$$\frac{\partial T}{\partial t} = \alpha \nabla^2 T - \Gamma \cdot [T - T_0] + R(T, C), \qquad (5.2)$$

which is the heat diffusion equation with a source term consisting of the two latter terms on the right-hand-side of the equation. The first of these is the convective heat loss described by Newtonian cooling (T_0 is the temperature of the surrounding air), and the second one is a heat generation term related to chemical reactions, i.e., slow combustion in this case. The convective heat transfer coefficient Γ is, in principle, dependent on the location of the front in a similar way as in Chapters 2.5 and 2.6. But as the effect of the correction term was quite small (see the inset of Fig. 2.9 on page 22), here we approximate Γ to be a constant.

The term $R(T, C)$ depends in a nonlinear way on the local temperature $T(x, y, t)$, and is proportional to the reactant concentration $C(x, y, t)$. In Ref. [8] this term was modeled as

$$R = \lambda_2 \frac{A^{3/2}}{\rho c_p} T^{3/2} e^{-A/T} C = -\lambda_1 \frac{\partial C}{\partial t}, \tag{5.3}$$

where A is the activation energy of the reaction (with the Boltzmann constant set to unity), ρ is the density and c_p the specific heat of air, and λ_1 and λ_2 are constants. As it turns out [8], Eqs (5.2) and (5.3) are equivalent to the KPZ equation, if short wavelength components in the fronts are not considered and the reactant concentration is nearly uniform. Because these criteria were met in our experiments, the slow-combustion fronts are considered from the perspective of KPZ dynamics in the following.

5.1 KPZ-type interfaces and their height-fluctuation distributions

The (squared) front width measures the roughness of an interface and is defined as

$$w^2(L, t) = \langle \overline{(h - \bar{h})^2} \rangle, \tag{5.4}$$

where the overbar denotes spatial and the brackets noise averaging. L is the system size in the x direction. For an initially flat interface that follows KPZ dynamics the roughness scales as $w \sim t^{1/3}$ at early times. Later, when the system becomes spatially correlated over the whole system length, L, a stationary state is reached as the roughness saturates on a certain level $w_L \sim L^{1/2}$ [29–31].

Exact results are available for height fluctuations of the KPZ type interfaces [32]. This problem is related to distributions of the largest eigenvalues of certain ensembles of random matrices. More specifically, if $h(x, t)$ is the position of the interface at point x at time t in a translationally invariant system, the probability distribution for local fluctuations of the position around its mean value is given by

$$P\left(\frac{h(x, t_2) - [h(x, t_1) + (t_2 - t_1)\langle \partial_t h \rangle]}{A_q(t_2 - t_1)^{1/3}} \leq s \right) = F_q(s), \tag{5.5}$$

where A_q is a constant depending on system-specific parameters, and $\langle \partial_t h \rangle$ is the average velocity of the interface in the time interval $t_1 < t < t_2$. The distribution function $F_q(s)$ depends on the global geometry of the average interface and also on its initial conditions: this distribution function is different for stationary and transient fluctuations meaning stationary and flat initial configurations of the interface, respectively.

For transient dynamics that evolve from the initial conditions $h(x, t_1) \equiv 0$ for all x, realized for times $t_1 < t_2 < t_{\text{sat}}$ with t_{sat} the time at which the stationary state is reached, the distribution function for fluctuation in the local position (height) of the interface is denoted by $F_1(s)$ in Ref. [32]. For a system in a stationary state, for which the times t_1 and t_2 defined above must satisfy $t_{\text{sat}} < t_1 < t_2$, this distribution function is denoted by $F_0(s)$ [32]. Expressions for the distribution functions $F_q(s)$ and the respective probability densities $f_q(s) = \mathrm{d}F_q(s)/\mathrm{d}s$ in both these cases can be found in Refs [32–36].

5.2 Slow-combustion front experiments

Ample experimental evidence had been provided [7, 37–40] that indicates the dynamics of slow-combustion fronts in paper asymptotically belong to the KPZ universality class. Therefore it was interesting to study also the height-fluctuation distributions in these fronts and try to verify existing theoretical results.

The experimental setup used was the one reported by Maunuksela et al. [37], and described in more detail in [7]. In brief, paper samples were made to smolder, with initially a linear combustion front, inside a chamber whose air flow could be controlled. A sample was attached to an aluminum frame with columns of thin pins pushed through folds at the vertical edges of the sample. The folds also compensated for the heat loss from the combustion front to the metallic pins. The frame was placed vertically in a chamber where air flow was directly upwards. Propagating fronts were recorded with three parallel black and white CCD cameras each having 768×548 pixels. The images were joined together and saved on-line on a hard drive for further processing and data analysis. The sample rate of the cameras was 2 images per second, i.e., $\Delta t = 0.5$ s, and the spatial resolution was 0.15 mm.

Copier paper of basis weight 80 g/m^2 and sample size 340 mm (width) by 600 mm was used in the experiments. To achieve flameless slow-combustion fronts, paper was impregnated with potassium nitrate that acted as an oxygen source. A dilute aqueous solution of KNO_3 was sprayed over the samples, after which the samples were dried in a press to maintain their planarity. Random small-scale variations in the concentration were obviously introduced by the spraying process. The average KNO_3 concentration of the samples varied between 1.3 and 1.9 g/m^2.

Ignition of the front was made with a tungsten wire heated by an electric current. The wire was stretched over the sample with two metallic strings to keep

its tension constant during heating, and to thereby get a linear front initially. The copier-paper samples were burned from top to bottom to minimize the convective heat transfer ahead of the front during its propagation.

Two initial conditions were used in the experiments: horizontal ignition and ignition with a slope of about ten degrees in the propagating fronts. The tilt angle used was only selected because it was convenient for the three-camera system. The angle was also chosen such that the system was not expected to be near the known phase boundaries for related models in the same universality class [41]. For the horizontal and tilted ignition a total of 18 and 21 successful burns were recorded, respectively.

5.3   Measured height fluctuation distributions

An example of combustion-front-height data for a horizontal ignition is shown in Fig. 5.1. Only the first half of the burn is shown, and the analysis window inside the transient regime (where $w \sim t^{1/3}$) is indicated by the lowest and highest of the thick lines. The front-height data from points close to the boundaries of the sample were excluded to avoid any boundary effects.
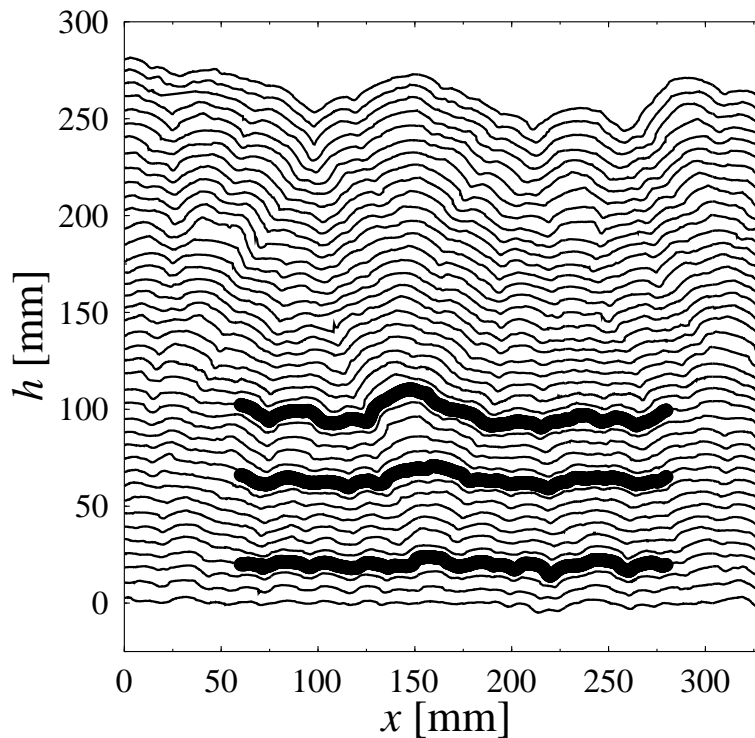

FIGURE 5.1 The first half of a horizontal burn. The analysis window used in the transient regime is indicated by the lowest and highest of the thick lines. In this particular case a pronounced avalanche in the middle of the burn was removed by lowering the upper limit of the analysis window. The time difference between the fronts shown is 10 s.

The height-fluctuation distribution determined for horizontal slow-combustion fronts in the transient regime is shown by dots in Fig. 5.2. The distribution is an average over individual burns. The average velocity $\langle \partial_t h \rangle$ in Eq. (5.5) was determined as a linear least-squares fit to the mean height as a function of time of the front. Within the indicated time interval, which was the interval over which the height-fluctuation averages were taken, these velocities varied in time. The front velocities averaged over the whole analysis intervals were also somewhat sample dependent. This caused the mean values of individual fluctuation distributions to differ from each other, and their direct summation would not have been meaningful. Because of this, the mean value was subtracted from every individual distribution before summation, and hence the experimental distribution has zero mean. This is why the theoretical f_1 distribution had to be transferred also to zero mean before fitting with it the transient height-fluctuation distribution.
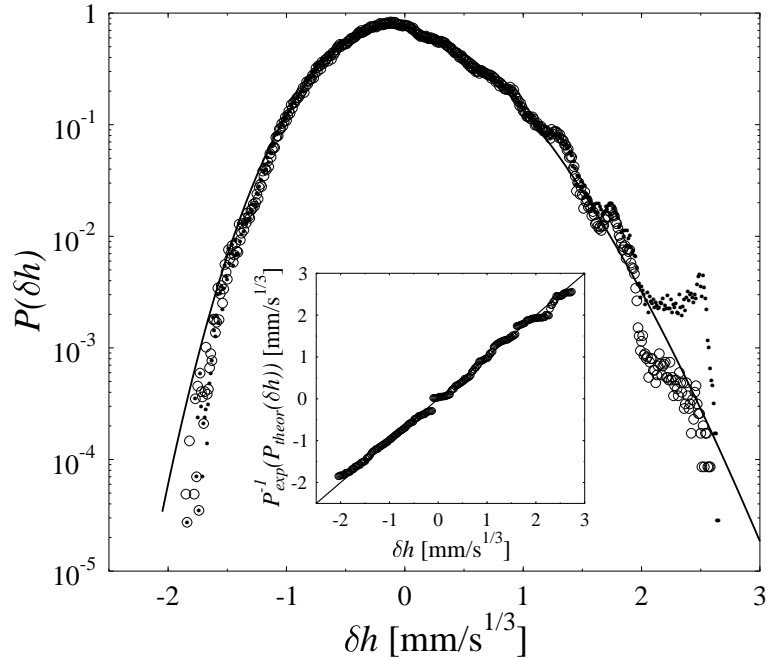

FIGURE 5.2 Height-fluctuation distribution for horizontal fronts in the transient ($w \sim t^{1/3}$) regime, and a fit by a (scaled and shifted) theoretical distribution f_1. A theoretical inversion of the measured distribution is shown in the inset. The dots denote the measured data and the circles the data with an avalanche suppressed.

Unexpected peaks appear at large positive fluctuations in Fig. 5.2. These peaks can be attributed to so called 'avalanches', i.e., to narrow intermittent parts of the front that rapidly advance ahead of the rest of it. This kind of behavior is triggered by quenched noise in the system (variations in the density of paper material and in the KNO_3 concentration), and would not be present in a pure KPZ system with uncorrelated white noise. In order to diminish the effect of such 'unwanted' avalanches on the height-fluctuation distribution, one distinct avalanche

was suppressed from the measured data (see Fig. 5.1). When the analysis window was reduced for the measurement containing an avalanche, the height-fluctuation distribution was well fitted by the theoretical distribution f_1 shown by a line in Fig. 5.2. The original [32–36] horizontal scale of the f_1 distribution was multiplied by a proper scaling factor, in this case by 0.67845. The scaling factor was selected such that the two distributions had equal variance after normalization. Because the mean value of the experimental distribution was zero as explained above, the fitted distribution was also shifted horizontally to zero mean. A theoretical inversion of the measured distribution is shown in the inset of Fig. 5.2, and it indicates close agreement of the experimental result with the theoretical distribution.
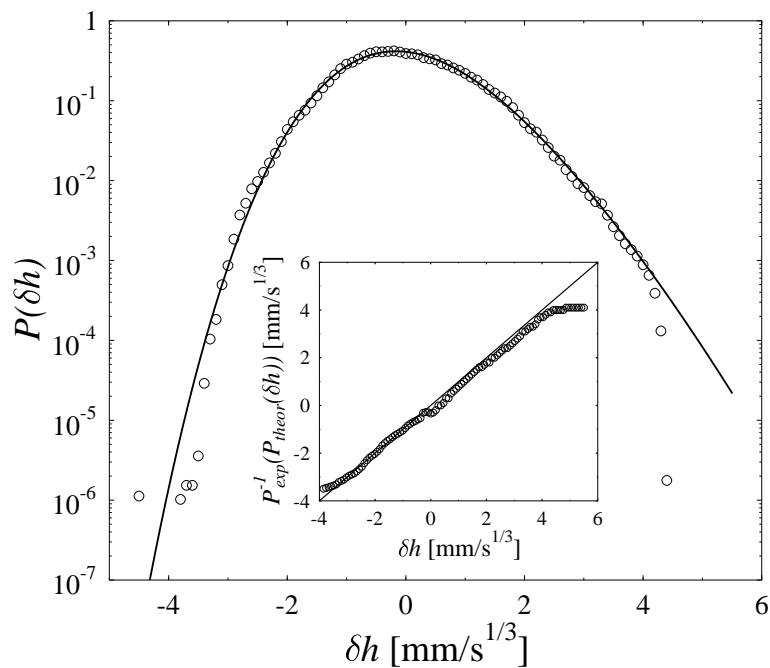

FIGURE 5.3 Height-fluctuation distribution for horizontal fronts in the saturated regime, and a fit by a (scaled) f_0 distribution.

Height-fluctuation distribution was also determined for saturated fronts (saturated width w_L). Figure 5.3 shows the distribution measured for horizontal fronts together with a fit by the theoretical f_0 distribution. It seems that, in the saturated regime, height fluctuations follow fairly closely the f_0 distribution. For large fluctuations, i.e., for large δh, the results fall below the theoretical distribution because of limited statistics and finite system size. The skewness of the measured distribution is 0.32 while that of a f_0 distribution is 0.359.

It is not possible to maintain indefinitely a tilted slow-combustion front with free boundaries because the front will gradually straighten as a λ term responsible for KPZ-type behavior will drive small-tilt fluctuations inwards from the up-hill boundary. The leading edge of the front thus tends to get retarded from its constant-average-tilt position (see Fig. 5.4). These boundary effects will eventually penetrate

the system and straighten out the whole front.

However, it is possible to study the behavior of the tilted part of a propagating front when an appropriate position window is applied in the analysis. There is an upper limit to the time scale during which it is possible to examine in this way a tilted front. This time scale obviously depends on system size.
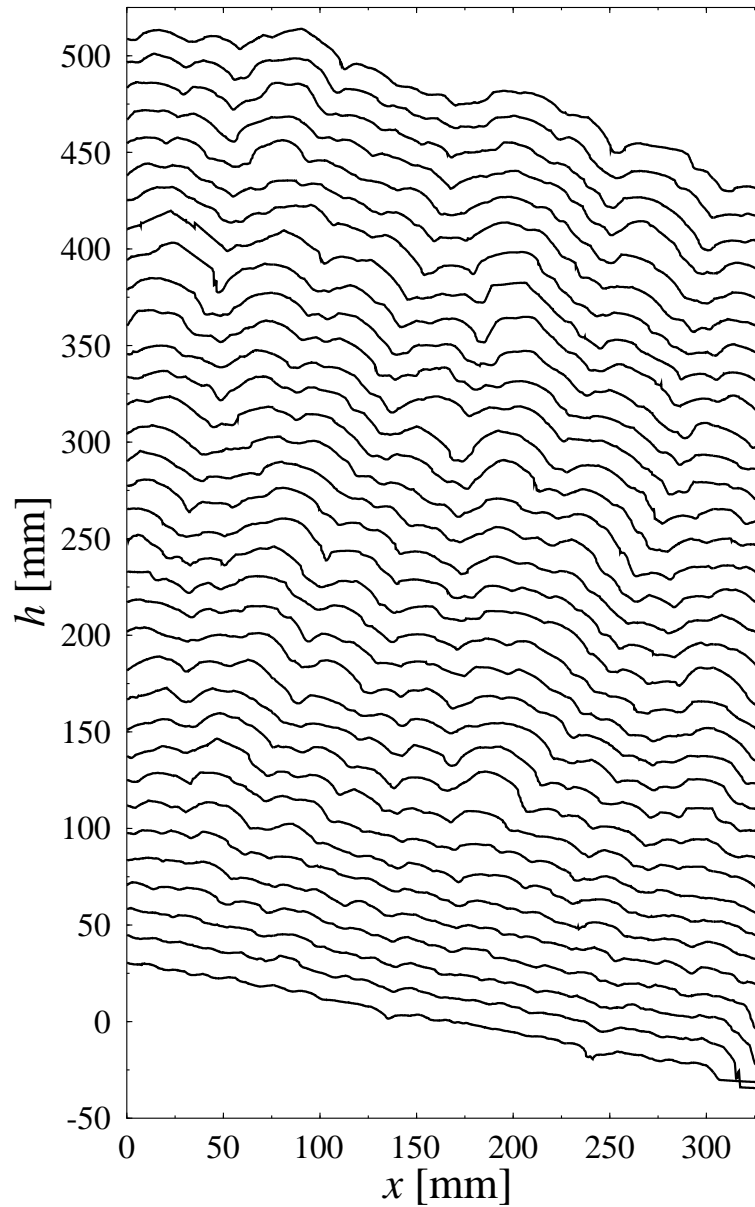

FIGURE 5.4 A slow-combustion burn for a tilted ignition with an average slope of ten degrees. The time difference between the fronts shown is 20 s. Penetration inwards of boundary effects is clearly visible.

The definition Eq. (5.4) of front roughness w is not quite consistent for tilted fronts, because the mean height $\bar{h}$ does not represent the 'average profile' of a front. Therefore, for tilted fronts, the front width was measured with respect to linear least-

squares fits of the fronts.

Figure 5.5 shows the height-fluctuation distribution measured for tilted fronts in the transient regime. These fluctuations were measured in the direction perpendicular to the tilted ignition front, i.e., the fronts of a tilted burn were rotated by 10 degrees before determining their height fluctuations. The skewness of the measured distribution is 0.33 while that of the f_1 distribution is 0.2935.
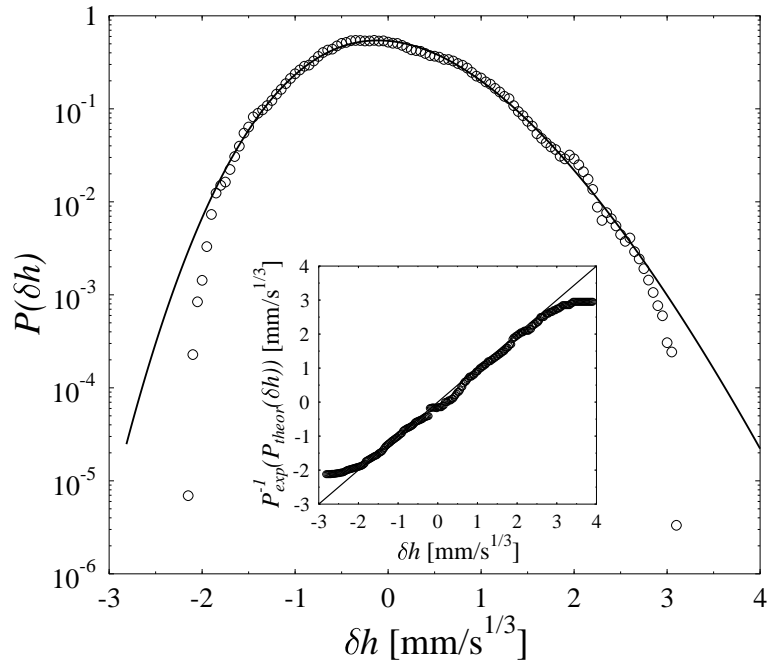

FIGURE 5.5 Height-fluctuation distribution for tilted fronts in the transient regime, and a fit by a (scaled and shifted) f_1 distribution.

The theoretical results reported for height-fluctuation distributions [32] were derived for infinite systems for which front width can grow without saturation. In real life the finite size of the system leads to a transient regime of finite duration before saturation sets in. Thus there will always be a cutoff in the measured amplitude of fluctuations in the front position, and the data will fall below the theoretical distribution at large δh.

Chapter 6

Conclusions

Measurement methods for determining the in-plane thermal diffusivity of planar samples were developed. The techniques used were based on heating a planar sample at one edge and recording the evolution of the temperature field of the sample by an infrared camera. The temperature fields at different times were averaged over a narrow strip at the center line of the sample for obtaining one-dimensional temperature profiles. These profiles were then fitted by a solution to a one-dimensional heat equation describing the experimental setup, thermal diffusivity as one of the fitting parameters.

The methods developed can be applied to good and moderate conductors of heat, as verified by measurements on metal samples. For good heat conductors it was sufficient to do the measurements in air, provided that all disturbing air flows were removed, i.e., the convective heat transfer from the sample was made constant. Both convective and radiative heat losses from the sample were taken into account in the heat equation that was used to describe the experimental setup.

The experimental setup was further improved by placing the sample in a vacuum chamber, where convective heat transfer was totally removed. After the measurement method was verified by measuring (metallic) samples with known thermal properties, the effective thermal conductivity of porous sintered bronze samples were determined. In addition to thermal conductivity measurements, the sintered samples were imaged with an X-ray microtomography scanner to obtain a detailed 3D model of the structure of each sample.

The analysis of the 3D reconstructions of the sintered bronze samples showed, together with the measured effective thermal conductivities, that the theoretical prediction $k_e/k_s \propto \sqrt{A_{contact}^{tot}/\pi} \cdot N_A/N_L$ did indeed reflect the behavior of a porous system. However, this simple theory does not include the possible effect of thermal contact resistance between particles. Limited resolution of the X-ray images induced contact area estimates larger than in reality, and therefore the simulated thermal conductivities were higher than measured. This effect could be taken into account in simulations by introducing thermal resistance between particles, and by reducing the area of contacts to the same effect in the theoretical prediction. An im-

portant conclusion of this result is that, in order to describe thermal conductivity, three structural parameters are needed, and there does not seem to be any simple relationship between thermal conductivity and porosity in heterogeneous porous systems. In regular structures many structural parameters are, however, connected.

One limitation of the measurement methods applied in this work is that the position dependence of the thermal conductivity cannot be obtained. Only average, or effective, thermal conductivity of a heterogeneous sample can be measured as in the case of the sintered bronze samples. But this information is often enough for porous but otherwise homogeneous materials.

The measurement method for thermal diffusivity in vacuum could be still improved by modifying the heating element such that the temperature field in the sample could be measured closer to the point of heating. This would enable measurements on poor heat conductors. It would also be interesting to study the effect of convection in more detail by varying the pressure in the chamber in a controllable way. Of course, then there would be three parameters to optimize when fitting temperature data if the radiative heat-loss term was not linearized.

The heat equation that was applied in the experimental determination of thermal conductivity provides also the theoretical framework for the propagation of slow-combustion fronts in planar materials. Mean field approximation of a certain heat equation has been shown to lead to the KPZ equation [8] for the evolution of the front line. We now know that the heat equation relevant to the problem also includes a radiative heat-transfer term and a position dependent coefficient in the convective heat-transfer term, both of which were neglected in the original derivation of the KPZ equation. We get the same result if the radiative heat-transfer term is linearized and the position dependence is neglected in the convective heat-transfer term. In the slow-combustion experiments reported here both these approximations are expected to be fairly good, but further work is needed to analyze their possible effects in more detail. In any case, the height-fluctuation distributions of slow-combustion fronts in paper were shown to be very similar to the ones derived for the KPZ universality class. They were clearly non-Gaussian and were well fitted by the f_1 distribution of Ref. [32] for the transient fronts and by the f_0 distribution for saturated fronts. Deviation from the KPZ behavior was observed only for the biggest fluctuations of the front position, and such fluctuations were obviously depleted in the measurement data because of limited system size.

Bibliography

[1] C. Argento and D. Bouvard, "Modeling the effective thermal conductivity of random packing of spheres through densification," *Int. J. Heat Mass Transfer*, vol. 39, pp. 1343–1350, 1996.

[2] W. L. Vargas and J. J. McCarthy, "Heat Conduction in Granular Materials," *AIChE Journal*, vol. 47, pp. 1052–1059, 2001.

[3] M. Wang and N. Pan, "Modeling and prediction of the effective thermal conductivity of random open-cell porous foams," *Int. J. Heat Mass Transfer*, vol. 51, pp. 1325–1331, 2008.

[4] W. Woodside and J. H. Messmer, "Thermal Conductivity of Porous Media. I. Unconsolidated Sands," *J. Appl. Phys.*, vol. 32, pp. 1688–1699, 1961.

[5] I. H. Tavman, "Effective thermal conductivity of granulous porous materials," *Int. Comm. Heat Mass Transfer*, vol. 23, pp. 169–176, 1996.

[6] M. Elsari and R. Hughes, "Axial effective thermal conductivities of packed beds," *Applied Thermal Engineering*, vol. 22, pp. 1969–1980, 2002.

[7] M. Myllys, J. Maunuksela, M. Alava, T. Ala-Nissilä, J. Merikoski, and J. Timonen, "Kinetic Roughening in Slow Combustion of Paper," *Phys. Rev. E*, vol. 64, p. 036101, August 2001.

[8] N. Provatas, T. Ala-Nissilä, M. Grant, K. R. Elder, and L. Piché, "Scaling, Propagation, and Kinetic Roughening of Flame Fronts in Random Media," *J. Stat. Phys.*, vol. 81, no. 3/4, pp. 737–759, 1995.

[9] Y. S. Touloukian, *Thermophysical Properties of Matter, Vol. 1: Thermal Conductivity – Metallic Elements and Alloys.* New York: Plenum Press, 1972.

[10] W. J. Parker, R. J. Jenkins, C. P. Butler, and G. L. Abbott, "Flash Method of Determining Thermal Diffusivity, Heat Capacity, and Thermal Conductivity," *J. Appl. Phys.*, vol. 32, pp. 1679–1684, September 1961.

[11] L. Vozár and W. Hohenauer, "Flash Method of measuring the thermal diffusivity. A review," *High Temp. High Press.*, vol. 35/36, pp. 253–264, 2003/2004.

[12] I. Philippi, J. C. Batsale, D. Maillet, and A. Degiovanni, "Measurement of thermal diffusivities through processing of infrared images," *Rev. Sci. Instrum.*, vol. 66, pp. 182–192, January 1995.

[13] F. Cernuschi, A. Russo, L. Lorenzoni, and A. Figari, "In-plane thermal diffusivity evaluation by infrared thermography," *Rev. Sci. Instrum.*, vol. 72, pp. 3988–3995, October 2001.

[14] B. Rémy, A. Degiovanni, and D. Maillet, "Measurement of the In-plane Thermal Diffusivity of Materials by Infrared Thermography," *Int. J. Thermophys.*, vol. 26, pp. 493–505, March 2005.

[15] F. M. White, *Fluid Mechanics*. McGraw–Hill, Inc., 6 ed., 2008.

[16] F. P. Incropera and D. P. DeWitt, *Fundamentals of Heat and Mass Transfer*. John Wiley & Sons, 5 ed., 2002.

[17] J. V. Beck and K. J. Arnold, *Parameter Estimation in Engineering and Science*. New York: Wiley, 1977.

[18] J. K. Carson, S. J. Lovatt, D. J. Tanner, and A. C. Cleland, "Thermal conductivity bounds for isotropic, porous materials," *Int. J. Heat Mass Transfer*, vol. 48, pp. 2150–2158, 2005.

[19] M. Kaviany, *Principles of Heat Transfer in Porous Media*. Springer, 2 ed., 1999.

[20] W. van Antwerpen, C. G. du Toit, and P. G. Rousseau, "A review of correlations to model the packing structure and effective thermal conductivity in packed beds of mono-sized spherical particles," *Nuclear Engineering and Design*, vol. 240, pp. 1803–1818, 2010.

[21] C. K. Chan and C. L. Tien, "Conductance of Packed Spheres in Vacuum," *J. Heat Transfer*, vol. 95, pp. 302–308, 1973.

[22] R. C. Gonzalez and R. E. Woods, *Digital Image Processing*. Prentice-Hall, Inc., 2 ed., 2002.

[23] D. Wolf-Gladrow, "A Lattice Boltzmann Equation for Diffusion," *J. Stat. Phys.*, vol. 79, pp. 1023–1032, 1995.

[24] M. Wang, J. He, J. Yu, and N. Pan, "Lattice Boltzmann modeling of the effective thermal conductivity for fibrous materials," *Int. J. Thermal Sciences*, vol. 46, pp. 848–855, 2007.

[25] Z. Hashin and S. Shtrikman, "A variational approach to the theory of the effective magnetic permeability of multiphase materials," *J. Appl. Phys.*, vol. 33, pp. 3125–3131, 1962.

[26] R. Landauer, "The electrical resistance of binary metallic mixtures," *J. Appl. Phys.*, vol. 23, pp. 779–784, 1952.

[27] S. Kirkpatrick, "Percolation and conduction," *Rev. Mod. Phys.*, vol. 45, pp. 574–588, 1973.

[28] M. Kardar, G. Parisi, and Y.-C. Zhang, "Dynamic Scaling of Growing Interfaces," *Phys. Rev. Lett.*, vol. 56, pp. 889–892, 1986.

[29] A.-L. Barabási and H. E. Stanley, *Fractal Concepts in Surface Growth*. Cambridge, UK: Cambridge University Press, 1995.

[30] T. Halpin-Healy and Y.-C. Zhang, "Kinetic Roughening Phenomena, Stochastic Growth, Directed Polymers and all that," *Phys. Rep.*, vol. 254, pp. 215–415, March 1995.

[31] P. Meakin, *Fractals, Scaling and Growth Far From Equilibrium*. Cambridge, UK: Cambridge University Press, 1998.

[32] M. Prähofer and H. Spohn, "Universal Distributions for Growth Processes in 1+1 Dimensions and Random Matrices," *Phys. Rev. Lett.*, vol. 84, pp. 4882–4885, May 2000.

[33] J. Baik and E. M. Rains, "Symmetrized random permutations," 1999.

[34] J. Baik and E. M. Rains, "Limiting Distributions for a Polynuclear Growth Model with External Sources," *J. Stat. Phys.*, vol. 100, pp. 523–541, 2000.

[35] C. A. Tracy and H. Widom, "The Distribution of the Largest Eigenvalue in the Gaussian Ensembles: $\beta = 1, 2, 4$," in *Calogero–Moser–Sutherland Models* (J. F. van Diejen and L. Vinet, eds.), CRM Series in Mathematical Physics 4, pp. 461–472, New York: Springer–Verlag, 2000.

[36] M. Prähofer, *Stochastic Surface Growth*. PhD thesis, Zentrum Mathematik, Technische Universität München, Munich, 2003.

[37] J. Maunuksela, M. Myllys, O.-P. Kähkönen, J. Timonen, N. Provatas, M. J. Alava, and T. Ala-Nissila, "Kinetic Roughening in Slow Combustion of Paper," *Phys. Rev. Lett.*, vol. 79, pp. 1515–1518, August 1997.

[38] J. Merikoski, J. Maunuksela, M. Myllys, and J. Timonen, "Temporal and Spatial Persistence of Combustion Fronts in Paper," *Phys. Rev. Lett.*, vol. 90, p. 024501, January 2003.

[39] J. Maunuksela, M. Myllys, J. Merikoski, J. Timonen, T. Kärkkäinen, M. S. Welling, and R. J. Wijngaarden, "Determination of the stochastic evolution

equation from noisy experimental data," *Eur. Phys. J. B*, vol. 33, no. 2, pp. 192–202, 2003.

[40] M. Myllys, J. Maunuksela, J. Merikoski, J. Timonen, and M. Avikainen, "KPZ equation with realistic short-range-correlated noise," *Eur. Phys. J. B*, vol. 36, no. 4, pp. 619–626, 2003.

[41] B. Derrida, "An exactly soluble non-equilibrium system: The asymmetric simple exclusion process," *Phys. Rep.*, vol. 301, pp. 65–83, 1998.